

See discussions, stats, and author profiles for this publication at: <https://www.researchgate.net/publication/6465841>

Optimizing the Photocatalytic Properties of Hydrothermal TiO₂ by the Control of Phase Composition and Particle Morphology. A Systematic Approach

ARTICLE in JOURNAL OF THE AMERICAN CHEMICAL SOCIETY · APRIL 2007

Impact Factor: 12.11 · DOI: 10.1021/ja067050+ · Source: PubMed

CITATIONS

264

READS

246

8 AUTHORS, INCLUDING:



Vincenzo Buscaglia

Italian National Research Council

167 PUBLICATIONS 3,570 CITATIONS

SEE PROFILE



Carmen Canevali

Università degli Studi di Milano-Bicocca

54 PUBLICATIONS 1,032 CITATIONS

SEE PROFILE



Stefano Polizzi

Università Ca' Foscari Venezia

140 PUBLICATIONS 3,199 CITATIONS

SEE PROFILE



Franca Morazzoni

Università degli Studi di Milano-Bicocca

119 PUBLICATIONS 2,227 CITATIONS

SEE PROFILE

Optimizing the Photocatalytic Properties of Hydrothermal TiO₂ by the Control of Phase Composition and Particle Morphology. A Systematic Approach

Andrea Testino,^{*,†} Ignazio Renato Bellobono,[‡] Vincenzo Buscaglia,[§]
Carmen Canevali,[†] Massimiliano D'Arienzo,[†] Stefano Polizzi,[⊥] Roberto Scotti,[†] and
Franca Morazzoni[†]

Contribution from the Department of Materials Science, University of Milano-Bicocca, Via R. Cozzi 53, I-20125 Milano, Italy, Department of Physical Chemistry, Environmental Research Centre, University of Milano, Via Golgi 19, I-20133 Milano, Italy, Institute for Energetics and Interphases, Department of Genova, National Research Council, Via De Marini, 6, I-16149 Genova, Italy, and Department of Physical Chemistry, University of Venezia, Via Torino 155/b, I-30172 Venezia, Italy

Received October 4, 2006; E-mail: andrea.testino@mater.unimib.it

Abstract: The possibility of controlling the photocatalytic activity of TiO₂ nanoparticles by tailoring their crystalline structure and morphology is a current topic of great interest. In this study, a broad variety of well-faceted particles with different phase compositions, sizes, and shapes have been obtained from concentrated TiOCl₂ solutions by systematically changing temperature, pH, and duration of the hydrothermal treatment. The guide to select the suitable experimental conditions was provided by thermodynamic modeling based on available thermochemical data. By combining the results of TEM, HRTEM, XRD, density, and specific surface area measurements, a complete structural and morphological characterization of the particles was performed. Correlation between the photocatalytic activity in the UV photodegradation of phenol solutions and the particle size was established. Prismatic rutile particles with length/width ratio around 5 and breadth of 60–100 nm showed the highest activity. The surface chemistry of the particles was also investigated. Treatments that decrease the surface acidity, such as washing the powders with ammonia solution and/or calcining at 400 °C, have detrimental effect on photocatalytic activity. The overall results suggest correlation between particle morphology and photocatalytic activity and indicate that both electron–hole recombination and adsorption at the surface can be rate-controlling processes. The systematic approach presented in this study demonstrates that a substantial improvement of the photocatalytic activity of TiO₂ can be achieved by a careful design of the particle morphology and the control of the surface chemistry.

1. Introduction

Titanium dioxide, TiO₂, is widely used in different applications because of its specific properties: photocatalytic activity, photovoltaic effect, medium dielectric permittivity, high chemical stability, and low toxicity. Photocatalytic and photovoltaic properties are influenced by surface area, crystallite size, phase composition, nature and concentration of lattice defects, and impurities. Thus, specific applications, such as dye-sensitized solar cells¹ (DSSC) or advanced photochemical applications,² require TiO₂ with well-controlled chemical and physical properties.

Titania exists in three crystalline forms: anatase (A), rutile (R), and brookite (B). In a number of applications, a specific

polymorph and a well-defined particle size^{3,4} are required; for example, hydrothermal anatase with primary particle size of 10–14 nm showed the best performance⁵ in DSSC. Contrasting results are reported about the influence of phase composition and particle size on the photocatalytic oxidative degradation of organic pollutants in air or water. Indeed, different authors reported that anatase works better than rutile,⁶ others showed the best results for rutile,^{7–9} and much experimental evidence supported the existence of a synergistic effect of anatase and rutile mixed phases in enhancing the photocatalytic activity.^{8,10–12}

(3) Aruna, S. T.; Tirosh, S.; Zaban, A. *J. Mater. Chem.* **2000**, *10*, 2388.

(4) Almquist, C. B.; Biswas, P. *J. Catal.* **2002**, *212*, 145.

(5) Barbè, C. J.; Arendse, F.; Comte, P.; Jirousek, M.; Lenzmann, F.; Shklover, V.; Grätzel, M. *J. Am. Ceram. Soc.* **1997**, *80*, 3157.

(6) Linsebigler, A. L.; Lu, G.; Yates, J. T., Jr. *Chem. Rev.* **1995**, *95*, 735.

(7) Watson, S. S.; Beydoun, D.; Scott, J. A.; Amal, R. *Chem. Eng. J.* **2003**, *95*, 213.

(8) Mills, A.; Lee, S.-K.; Lepre, A. *J. Photochem. Photobiol., A* **2003**, *155*, 199.

(9) Habibi, M. H.; Vosoughian, H. *J. Photochem. Photobiol., A* **2005**, *174*, 45.

(10) (a) Bacsa, R. R.; Kiwi, J. *Appl. Catal. B* **1998**, *16*, 19. (b) Gumy, D.; Morais, C.; Bowen, P.; Pulgarin, C.; Giraldo, S.; Hajdu, R.; Kiwi, J. *Appl. Catal. B* **2006**, *63*, 76.

[†] Department of Materials Science, University of Milano-Bicocca.

[‡] Department of Physical Chemistry, Environmental Research Centre, University of Milano.

[§] Institute for Energetics and Interphases, Department of Genova, National Research Council.

[⊥] Department of Physical Chemistry, University of Venezia.

(1) Grätzel, M. *Nature* **2001**, *414*, 338.

(2) Zhang, W. F.; Zhang, M. S.; Yin, Z.; Chen, Q. *Appl. Phys. B* **2000**, *70*, 261.

While some authors claimed that high surface area or mesoporous materials have higher efficiency,^{10,13} some others pointed out the influence of crystalline and surface defects.¹⁴ In general, phase composition, specific surface area, pore size distribution, particle morphology, particle aggregation, primary and secondary particle size distribution, bulk, and surface defects, bulk and surface hydroxyl groups,^{15,16} and impurities¹⁷ can play a crucial role in determining the efficiency in specific applications. All the above-mentioned characteristics are directly associated to synthesis and processing routes. The shortcoming of the previous investigations to provide a self-consistent picture that effectively correlates phase composition and particle morphology to photocatalytic activity largely lies in the use of powders coming from different synthesis routes and different synthesis conditions.

Therefore, the first step toward a better understanding of the influence of the different parameters on the material performances is the selection of a preparation route able to supply TiO₂ with controlled and reproducible properties. Titania can be prepared by various methods, such as sol–gel,¹¹ hydrothermal,^{14,18} combustion synthesis,¹⁶ and gas-phase methods.^{19–20} Among these preparation methods, a careful control over phase composition and particle size and hence over photocatalytic activity can be obtained by means of the hydrothermal method. In general, this is carried out by changing the chemico-physical parameters of the system, such as temperature, pH, kind and concentration of reactants. Scale-up problems of the hydrothermal process—often related to lack of homogeneity in big reactors—can be resolved by the application of specific strategies.^{21–23}

In this study, we report the results of an extensive investigation on the hydrothermal synthesis of TiO₂ using aqueous TiOCl₂ and NH₄OH as reactants. Traditionally, the process parameters are empirically adjusted by trial-and-error until the given phase or particle size is obtained. It is generally reported that at basic pH the main or exclusive phase is anatase, while at acidic pH, rutile formation is favored.^{18,24–25} Herein, we propose a more systematic and quantitative approach. First, phase-stability diagrams were generated by using thermodynamic modeling to understand which ionic species in equilibrium with the solid phase predominates as a function of pH, temperature, and reactant concentration. Second, appropriate temperatures for the hydrothermal synthesis were selected, and TiO₂ powders were produced by systematically varying the pH

of the solution and the reaction time. The resulting products were fully characterized, and the effect of temperature, pH, and reaction time on phase composition, crystal size, and morphology was determined.

The photocatalytic activities of the different titania samples in the mineralization of phenol in the presence of H₂O₂ were measured and correlated with the size, morphology, and composition of the particles. The photocatalytic activity can be also controlled by changing the surface chemistry of the powders. For this purpose, a study on the influence of different washing treatments and thermal annealing was carried out. As a result, the synthesis and processing conditions corresponding to optimized photocatalytic activity were identified.

2. Thermodynamic Modeling

Precipitation and hydrothermal synthesis involve chemical reactions between ions or molecular species in aqueous solution and one or more solid phases. The chemical composition as well as the properties of the solid phases can be controlled by changing the physical and chemical variables of the given system, such as temperature, pressure, pH, reactant concentration. Phase-stability diagrams are very useful to understand which aqueous and solid phases predominate as a function of pH and reactant concentration. Thus, the optimum synthesis conditions for which the desirable product is thermodynamically stable can be predicted using a suitable thermodynamic model, without the need of a time-consuming trial and error experimental approach. Examples of the use of thermodynamic modeling for the hydrothermal synthesis of ceramic oxides have been provided by Lencka and Riman.^{26–28}

Here, we propose a similar approach for the system TiO₂–H₂O–HCl–NH₃ where modifications in morphology, growth rate, and phase composition of the solid phase can be related to a change of the predominant aqueous species or variations of the precipitate solubility. The calculations were based on a realistic activity coefficient model of aqueous solutions.²⁶ In fact, the ideal solution model is highly inaccurate when concentrated electrolyte solutions are used or when a multitude of competing reactions occur in a solution, making the equilibrium concentration of various species strongly dependent on activity coefficients. The distribution of the aqueous species was predicted as a function of temperature and pH. Calculations were performed with the OLI System software.²⁹

According to the general principles of chemical thermodynamics, the equilibrium concentration of the different species in the system can be calculated, provided that the standard Gibbs energy of formation and the activity coefficient are known for each species.^{26–28} Overall, 23 chemical species and 18 independent reactions were considered in the TiO₂–H₂O–HCl–NH₃ system, as shown in Scheme S1 (Supporting Information). At the titanium concentration used in the present study (0.45 mol/kg), mononuclear Ti(IV) species are probably predominant,³⁰ and a number of these species were considered. It is known that Ti(IV) species in aqueous solution are octahedrally coordinated. Ionic ligands, such as OH[–] and Cl[–], are commonly

- (11) Watson, S.; Beydoun, D.; Scott, J.; Amal, R. *J. Nanopart. Res.* **2004**, *6*, 193.
- (12) Yan, M.; Chen, F.; Zhang, J.; Anpo, M. *J. Phys. Chem. B* **2005**, *109*, 8673.
- (13) Peng, T.; Zhao, D.; Dai, K.; Shi, W.; Hirao, K. *J. Phys. Chem. B* **2005**, *109*, 4947.
- (14) Yin, H.; Wada, Y.; Kitamura, T.; Kambe, S.; Murasawa, S.; Mori, H.; Sakata, T.; Yanagida, S. *J. Mater. Chem.* **2001**, *11*, 1694.
- (15) Vorontsov, A. V.; Altyinnikov, A. A.; Savinov, E. N.; Kurkin, E. N. *J. Photochem. Photobiol., A* **2001**, *144*, 193.
- (16) Nagaveni, K.; Sivalingam, G.; Hegde, M. S.; Madras, G. *Appl. Catal., B* **2004**, *48*, 83.
- (17) Deng, X.; Yue, Y.; Gao, Z. *Appl. Catal., B* **2002**, *39*, 135.
- (18) Cheng, H.; Ma, J.; Zhao, Z.; Qi, L. *Chem. Mater.* **1995**, *7*, 663.
- (19) Jones, A. C.; Chalker P. R. *J. Phys. D: Appl. Phys.* **2003**, *36*, R80.
- (20) Wang, W.-N.; Lenggoro, I. W.; Terashii, Y.; Kim, T. O.; Okuyama, K. *Mat. Sci. Eng. B* **2005**, *123*, 194.
- (21) Hakuta, Y.; Ura, H.; Hayashi, H.; Arai, K. *Ind. Eng. Chem. Res.* **2005**, *44*, 840.
- (22) Jongen, N.; Testino, A. Patent, International Publication Number WO 2005/097705 A1, 2005.
- (23) Chaudhry, A. A.; Haque, S.; Kellici, S.; Boldrin, P.; Rehman, I.; Khalid, F. A.; Darr, J. A. *Chem. Commun.* **2006**, 2286.
- (24) Yanqing, Z.; Erwei, S.; Zhizhan, C.; Wenjun, L.; Xingfang, H. *J. Mater. Chem.* **2001**, *11*, 1547.
- (25) Song, K. C.; Pratsinis, E. *J. Am. Ceram. Soc.* **2001**, *84*, 92.

- (26) Lencka, M. M.; Riman, R. E. *Chem. Mater.* **1993**, *5*, 61.
- (27) Lencka, M. M.; Riman, R. E. *Chem. Mater.* **1995**, *7*, 18.
- (28) Lencka, M. M.; Anderko, A.; Riman, R. E. *J. Am. Ceram. Soc.* **1995**, *78*, 2609.
- (29) OLI Analyzer, V 1.3; OLI System Inc.: Morris Plains, NJ, 2004, (<http://www.olisystems.com>).
- (30) Reichmann, M. G.; Bell, A. T. *Langmuir* **1987**, *3*, 111.

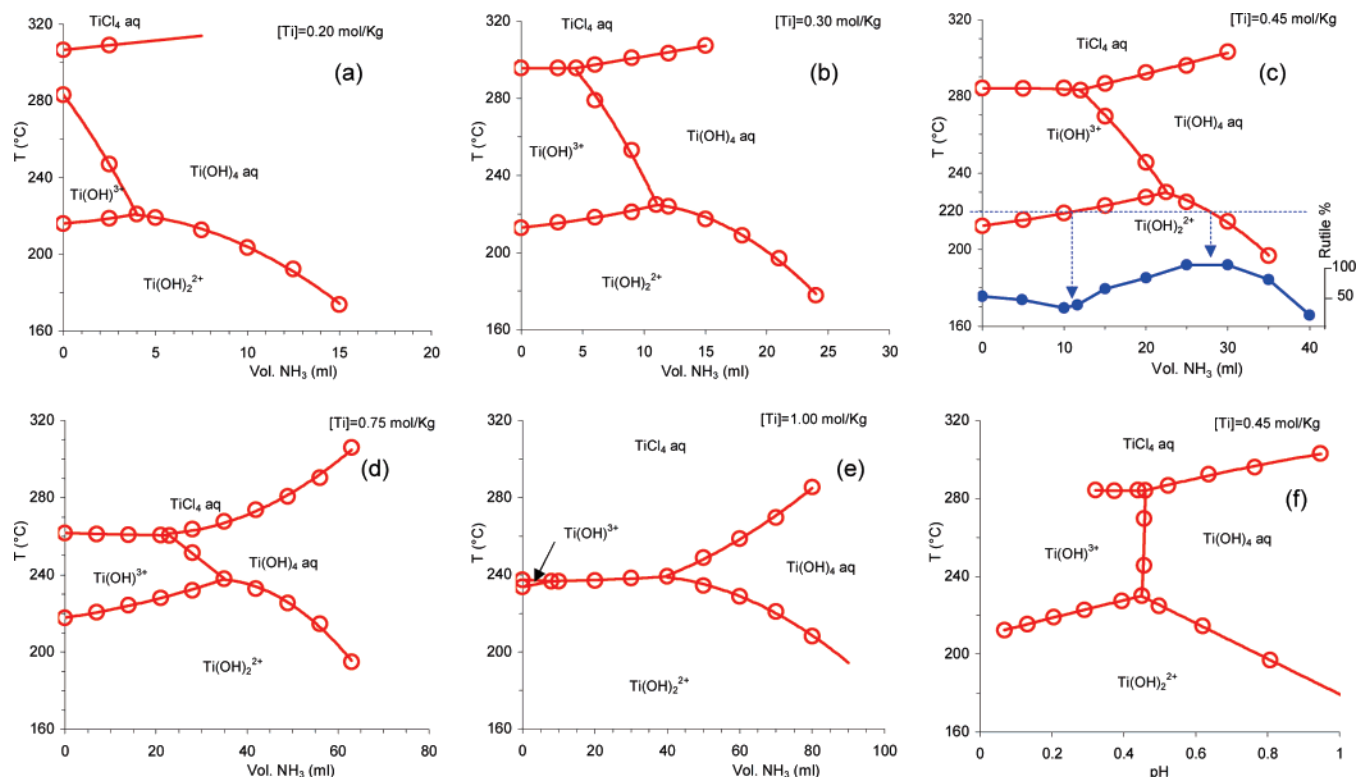


Figure 1. Stability diagrams of the predominant aqueous species in the $\text{TiO}_2/\text{NH}_3/\text{HCl}/\text{H}_2\text{O}$ system calculated for different values of the overall Ti concentration. (a) 0.20; (b) 0.3; (c) 0.45; (d) 0.75; (e) 1.00; (f) 0.45 mol/kg. (Inset (c): blue lines experimental rutile content for $T_R = 220^\circ\text{C}$ and reaction time = 2 h).

bound to Ti, and water molecules may complete the vacant octahedral positions. Therefore the $[\text{Ti}(\text{OH})_n]^{(4-n)+}$ and $[\text{TiCl}_n]^{(4-n)+}$ species (Scheme S1, Supporting Information) should be written as $[\text{Ti}(\text{OH})_n(\text{H}_2\text{O})_{6-n}]^{(4-n)+}$ and $[\text{TiCl}_n(\text{H}_2\text{O})_{6-n}]^{(4-n)+}$. An important species in concentrated and strongly acidic solutions is also the titanyl ion,³¹ TiO^{2+} . With increasing acid and/or titanium concentration, there is some experimental evidence that the mononuclear species condense to form oligomers containing Ti—O—Ti bonds.^{32,33} However, there are no thermodynamic data available for these species. Table S1 (Supporting Information) shows the standard thermodynamic properties²⁹ used in the equilibrium calculations; the activity coefficients were computed by means of the OLI System software according to the approach described in ref 26. As initial conditions, the solution of TiOCl_2 in water was treated as a mixture of $\text{Ti}(\text{OH})_4(\text{aq})$ and $\text{HCl}(\text{aq})$ according to the irreversible reaction 1 in Scheme S1 (Supporting Information). The initial amount of HCl was given by the experimental $\text{H}^+/\text{Ti}^{\text{IV}}$ molar ratio (see section 3.1).

It is well-known that R is thermodynamically more stable than A. However, when crystals are nanosized, rutile is less stable than anatase.^{34–36} Thus, only anatase is observed below the critical size of 11–16 nm. The model used in the thermodynamic calculations does not take into account the particle size, and all calculations were carried out with A as solid phase. Replacement of A with R did not produce any significant effects on the stability diagrams. The effect of particle size on the solubility of the solid phase was evaluated *a*

posteriori by means of the Gibbs–Thompson equation, as shown later.

The calculations were carried out at different reaction temperatures (T_R) in the range 20–300 °C and for several values of titanium concentration (0.2–1 mol/kg). Herein, the concentration is always expressed as number of moles per kilogram of solution, molality. The pH was adjusted by simulating the addition of increasing volumes (V_A) of ammonia solution. The pressure in the hydrothermal reactor was assumed to be the equilibrium vapor pressure of pure water (autogenous pressure) at the given temperature. This assumption was experimentally verified. Three different plots were then generated from the calculated equilibrium concentrations: (i) the stability diagrams which show the predominant aqueous species in equilibrium with solid anatase as a function of T_R and V_A (or pH); (ii) the pH of the hydrothermal suspension as a function of T_R and V_A ; (iii) the solubility of TiO_2 as a function of T_R and V_A . Case (i) is described in more detail.

(i) The stability diagrams for the aqueous species, generated for different values of the overall titanium concentration (0.20–1.0 mol/kg), show the predominant aqueous species as a function of T_R and V_A (Figure 1a–e) or pH (Figure 1f). Only the portion of the diagrams corresponding to strongly acidic pH was reported.

The lines on the diagrams represent the loci of points where two predominant aqueous species have the same concentration and, consequently, they divide the diagram in several regions, each corresponding to a different predominant species. Over 10 different titanium species were taken into account in the calculations (Scheme S1 and Table S1, Supporting Information), but there are only four predominant species in the range of temperature, pH, and concentration examined. The increase of

(31) Grätzel, M.; Rotzinger, F. P. *Inorg. Chem.* **1985**, 24, 2320.

(32) Comba, P.; Merbach, A. *Inorg. Chem.* **1987**, 26, 1315.

(33) Reichmann, M. G.; Hollander, F. J.; Bell, A. T. *Acta Crystallogr.* **1987**, C43, 1681.

(34) Hu, Y.; Tsai, H.-L.; Huang, C.-L. *Mater. Sci. Eng., A* **2003**, 344, 209.

(35) Zhang, H.; Banfield, J. F. *J. Mater. Chem.* **1998**, 8, 2073.

(36) Zhang, H.; Banfield, J. F. *J. Phys. Chem. B* **2000**, 104, 3481.

TiO₂ solubility caused by the small particles size was not considered in the calculation of the stability diagrams because it has only a minor effect on the location of the predominance regions.

An increase of the overall amount of Ti leads to an increase of the concentration of Cl[−] and H⁺ and of the ionic strength. These variations determine the modification of the stability diagrams observed in Figure 1a–e. Namely, the predominance region of TiCl₄(aq), progressively extends toward lower temperatures, while the predominance region of Ti(OH)³⁺(aq) shrinks.

(ii) The pH of the hydrothermal suspension as a function of the added ammonia volume was calculated for a Ti concentration of 0.45 mol/kg. The variation of pH with temperature is mainly the consequence of the temperature dependence on the water ionic product, $a_{\text{H}^+} a_{\text{OH}^-}$, where a denotes the activity (Figure S1, Supporting Information). The variation of pH with V_A is slow and progressive until the equivalent point is approached. The calculated equivalence point corresponds to $V_A \approx 42$ mL (inset in Figure S1).

(iii) The solubility of TiO₂ was calculated for a Ti concentration of 0.45 mol/kg (Figures S2–S3, Supporting Information). The solubility strongly decreases with increasing temperature and pH. It turns out that quantitative precipitation of TiO₂ (solubility <0.01 mol/kg) occurs above 100 °C in the experimental conditions adopted in the present study. Figure S2a shows the equilibrium solubility of TiO₂ neglecting the influence of the particle size. However, the solubility of nanoparticles is strongly enhanced by their small dimension, as predicted by the Gibbs–Thompson equation³⁷ (see Figure S2, Supporting Information). A value of 0.5 J m^{−2} was assumed in the calculations for the solid–liquid surface energy, according to the results of first-principles calculations^{38,39} for low-energy surfaces of anatase (0.44 J m^{−2} for {101} and 0.53 J m^{−2} for {100}). Extrapolation from the data reported by Barnard and Curtiss⁴⁰ gives an average surface energy for anatase of 0.53 J m^{−2} for strongly acidic surfaces.

The results of the calculation for anatase nanoparticles with a diameter of 12 nm are shown in Figure S2b. The observed trends are in general agreement with the solubility results reported in literature.⁴¹ The increase of solubility is significant, about 2 orders of magnitude near room temperature and about 1 order of magnitude at 300 °C. Nevertheless, complete precipitation of TiO₂ (solubility <0.01 mol/kg) is predicted above 140 °C. TiO₂ solubility as a function of V_A is reported in Figure S3 (Supporting Information). As with the pH (Figure S1), the calculated solubility shows a slow and progressive variation until the equivalent point is approached.

3. Experimental Section

3.1. Synthesis of TiO₂. All chemical reagents were commercial products used without further purification. The Ti content of the TiOCl₂ aqueous solution (Aldrich, 99%) was determined as TiO₂ by gravimetric analysis and was 3.16 mol/kg. The reactant acidity was titrated with KOH, and the H⁺/Ti^{IV} molar ratio was determined to be 3.84 mol/mol. The ammonia solution (Fluka, >25 wt.%) was titrated with HCl, and

the resulting NH₃ titer was 28.0 wt.%. The water used in the experiments was always freshly distilled water.

The required amount of TiOCl₂ was weighed in a 500-mL polyethylene bottle and diluted with water under stirring. The NH₃ solution was slowly added at room temperature (5 mL min^{−1}) under stirring. The overall amount of water (partly used for dilution and partly contained in the ammonia solution) was that required to have an overall mass of 360 g for each experiment and a Ti concentration of 0.45 mol/kg. All reagents were weighed with the accuracy of ±0.01 g. The solution was vigorously stirred by a magnetic stirrer and immediately transferred into a 600-mL Teflon-lined autoclave (Parr, model 4768Q). The temperature during the hydrothermal treatment was measured by means of a Teflon-coated thermocouple immersed in the solution. The autogenous pressure was measured by means of an external transducer. Magnetic stirring was applied during the whole hydrothermal process. The autoclave was heated at 2.67 °C/min to a temperature of 30 °C below the setup temperature and then at 0.75 °C/min up to the maximum temperature (reaction temperature T_R). The suspension was then aged for a given reaction time, t_R , (1–6 h) with a maximum temperature fluctuation of −1/+4 °C. The autoclave was cooled in air outside the oven until the temperature dropped below 70 °C. The suspension was then recovered from the autoclave and concentrated by natural decantation. If not otherwise specified, the final powder was washed first with water, then with ammonia solution, and finally with acetone and was recovered by filtration and dried under vacuum at room temperature. The samples were labeled as SN where N is a progressive number. Samples labeled with H, e.g., SNH, did not undergo ammonia washing. Samples labeled with T, e.g., SNT, were further calcined at 400 °C for 2 h in air.

3.2. Powder Characterization. X-ray diffraction (XRD) patterns of the powders were collected with a Philips PW1710 diffractometer (Co K α radiation, voltage 40 kV, current 30 mA, secondary graphite monochromator) in the range 20–80° 2 θ (2 θ step 0.025°, count time of 2 s per step). Calculation of unit cell parameters and polymorph composition was performed by the Rietveld method using the GSAS⁴² software and the ICSD⁴³ database as reference. The crystallite size, L_{XRD} , of TiO₂ was estimated from the broadening of the XRD peaks by means of the Scherrer equation, after correction for instrumental broadening, assuming negligible microstrain broadening. The peaks used for the calculation were 110 for R, 101 for A, and 211 for B.

High-resolution transmission electron microscopy (HRTEM) and electron diffraction (ED) were performed using a Jeol 3010 apparatus operated at 300 kV with a high-resolution pole piece (0.17 nm point-to-point resolution) and equipped with a Gatan slow-scan 794 CCD camera. The powders were suspended in isopropanol, and a 5 μ L drop of this suspension was deposited on a holey carbon film supported on 3-mm copper grid for TEM investigation.

Scanning electron microscopy (SEM) observations were performed using a LEO 1450VP instrument.

The density, ρ , of the powders was measured by helium pycnometry (Micromeritics, Accupyc 1330) after drying the samples at 200 °C for 1 h.

The specific surface area (BET method⁴⁴), A_{BET} , and the pore size distribution (BJH method, desorptions branch⁴⁵) were determined by nitrogen physisorption (Micromeritics, ASAP 2010), after evacuation at 200 °C for 12 h.

UV–vis diffuse reflectance spectra (DRS) were obtained on pellets of pressed powders using a Perkin-Elmer Lambda 900 spectrometer equipped with an integrating sphere and employing a Spectralon diffuse reflectance standard.

- (37) Sugimoto, T. *Adv. Colloid Interface Sci.* **1987**, *28*, 65.
(38) Lazzeri, M.; Vittadini, A.; Selloni, A. *Phys. Rev. B* **2001**, *63*, 155409.
(39) Lazzeri, M.; Vittadini, A.; Selloni, A. *Phys. Rev. B* **2002**, *65*, 119901(E).
(40) Barnard, A. S.; Curtiss, L. A. *Nanoletters* **2005**, *5*, 1261.
(41) Schmidt, J.; Vogelsberger, W. *J. Phys. Chem. B* **2006**, *110*, 3955.

- (42) Larson, A. C.; Von Dreele, R. B. *General Structure Analysis System (GSAS)*, Technical Report LAUR 86-748; Los Alamos National Laboratory: New Mexico, 2000.
(43) Inorganic Crystal Structure Database (ICSD), Fachinformationzentrum Karlsruhe and Gemlin Institute, Karlsruhe (1997): Anatase #202242; Brookite #36411; Rutile #64987.
(44) Brunauer, S.; Emmet, P. H.; Teller, E. *J. Am. Chem. Soc.* **1938**, *60*, 309.
(45) Barret, E. P.; Joyner, L. G.; Halenda, P. P. *J. Am. Chem. Soc.* **1951**, *73*, 373.

3.3 Photocatalytic Activity. Photodegradation experiments were carried out in a 400-mL pyrex discontinuous batch reactor with an external cooling jacket and equipped with a UV 125-W Hg high-pressure lamp placed in a coaxial quartz cylinder. No optical filter was adopted. The reactor was externally enveloped by an aluminum foil.

Titanium dioxide (100 ± 5 mg) was suspended by sonication in 400 mL of an aqueous solution containing phenol (PhOH) with concentration of 121 ± 2 ppm (93 ± 2 ppm as C). Then, a stoichiometric amount of a 35 wt % H_2O_2 solution was added ($\text{PhOH}/\text{H}_2\text{O}_2 = 14 \pm 0.01$ mol/mol), the suspension stirred in the dark for 30 min, and then the UV source was turned on. The temperature of the suspension was kept at 25 ± 2 °C. The photoinduced degradation of phenol was monitored by withdrawing suspension aliquots (6 mL) at regular intervals. The TiO_2 powder was separated from the solution by centrifugation. The clear solution was analyzed for the total organic carbon (TOC). Reference experiments were performed in the absence of TiO_2 (blank) as well as by using Degussa P25 titanium dioxide as photocatalyst. TOC was determined using a Shimadzu TOC-V CSH analyzer.

4. Results

4.1 Powder Characterization: Phase Composition, Morphology, Specific Surface Area, Band Gap. Forty titania samples corresponding to different experimental conditions (T_R , V_A , t_R) were synthesized and fully characterized (see Table S2, Supporting Information). Hydrothermal treatments were mainly carried out at 160 and 220 °C for 2 and 6 h. Some experiments were also performed at lower temperature or for a shorter time. Below 100 °C and short aging times, the reaction product was mainly composed of anatase with crystallite size <5 nm (Sample S0, Table S2, Supporting information). Some preparations were repeated two or three times to evaluate the reproducibility of the process. The estimated variance in the phase composition was of the order ± 5 wt%.

4.1.1. Phase Composition and Particle Morphology. Figure 2 shows the XRD patterns of some selected products as typical examples of both single and mixed TiO_2 phases. It is worth noting that, at $T_R = 220$ °C (patterns a–f) and depending on V_A , the synthesis can be directed toward the production of pure rutile (30 mL), pure anatase (50 mL), or a phase mixture (0–25 and 30–45 mL). When $V_A = 20$ mL (patterns g–l), anatase is the predominant product at 110–130 °C, whereas pure rutile is obtained at 220–250 °C. For all samples, the calculated lattice parameters agree with the ICSD reference values⁴³ within the experimental error (± 0.002 Å). This indicates that the concentration of lattice defects, such as hydroxyl ions, is relatively low. In agreement, no significant density differences are observed between as-prepared and calcined (400 °C) powders. Moreover, the experimental density and the theoretical density calculated from the unit cell volume agree within 1–3% (see Table S2, Supporting Information).

TEM and HRTEM images of some representative samples are reported in Figure 3. No internal pores or amorphous surface layers were detectable. Particles are single nanocrystals, with pronounced faceting, or ordered aggregates probably originated by oriented attachment of primary nanocrystals. Rutile particles show elongated prismatic shape with an aspect ratio α ($\alpha = \text{length/width}$) of about 5 (see Figure 3a); they grow in the $[001]$ direction and form aggregates with shared $\{110\}$ faces^{46,47}

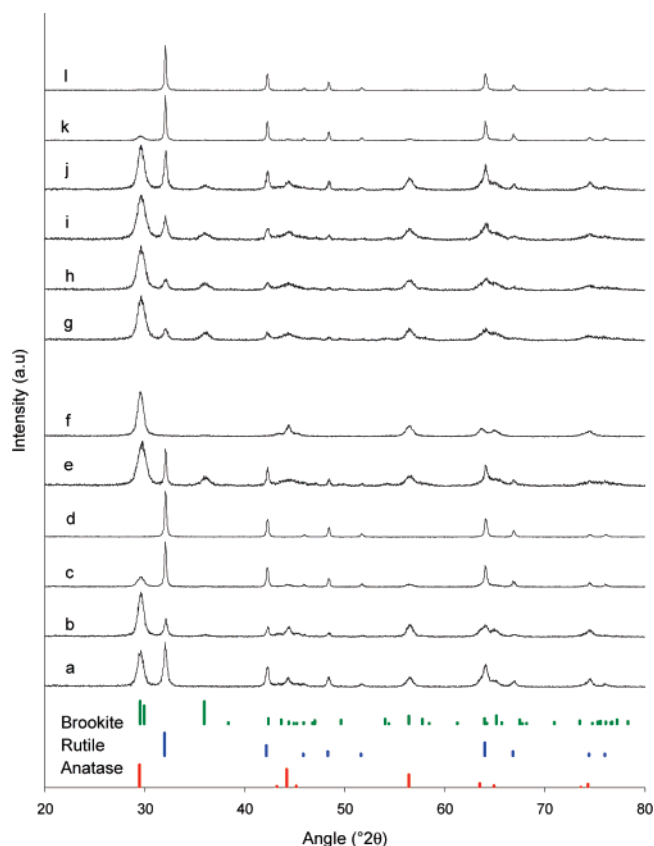


Figure 2. XRD patterns of samples obtained from a TiOCl_2 solution with concentration of 0.45 mol/kg after hydrothermal treatment for 2 h. (a–f) $T_R = 220$ °C and $V_A = 0, 10, 20, 30, 40, 50$ mL from a to f. (g–l) $V_A = 20$ mL and $T_R = 109, 132, 161, 184, 220, 250$ °C from g to l. The vertical lines indicate position and intensity of A, R, and B reflections. Note that (c) and (k) correspond to the same synthesis conditions but are two different repetitions.

(Figure 3b); the facets at the end of the prisms can be $\{011\}$ (see section 5). For relatively long aging times (e.g., 6 h, sample S16, Figure 4) the particle size distribution becomes broader, and mean α value decreases. As the rutile crystals grow along the c -axis, the size L_{XRD} calculated from the broadening of the 110 peak corresponds to the width of the crystals. Anatase particles (Figure 3c) are more equiaxed, and the fringes corresponding to the (101) crystallographic planes are most frequently observed. According to ref 48, the faces exposed are the $\{010\}$ oriented perpendicular to the planes (101). The aspect ratio of A particles is 1–3 for most of the particles with a smaller number of longer particles (Figure 3e). The (101) lattice fringes are generally parallel to the direction of elongation of the anatase nanocrystals (inset Figure 3c); therefore, the size L_{XRD} calculated from the 101 peak corresponds to the particle width. The morphology of some of the elongated anatase particles, presenting steps and dimples, suggests growth by oriented attachment of primary nanocrystals along the $[101]$ direction and other directions (Figure 3d,e) (see section 5). However, as for the rutile particles, it is not clear if oriented aggregation has occurred during the hydrothermal treatment or as a consequence of the drying treatment. The particle morphology was practically independent of the phase composition of

(46) Wu, J.-M.; Zhang, T.-W. *Langmuir* **2005**, *21*, 6995.

(47) Hosono, E.; Fujihara, S.; Kakiuchi, K.; Imai, H. *J. Am. Chem. Soc.* **2004**, *126*, 7790.

(48) Shklover, V.; Nazeeruddin, M.-K.; Zakeeruddin, S. M.; Barbé, C.; Kay, A.; Haibach, T.; Steurer, W.; Hermann, R.; Nissen, H.-U.; Grätzel, M. *Chem. Mater.* **1997**, *9*, 430.

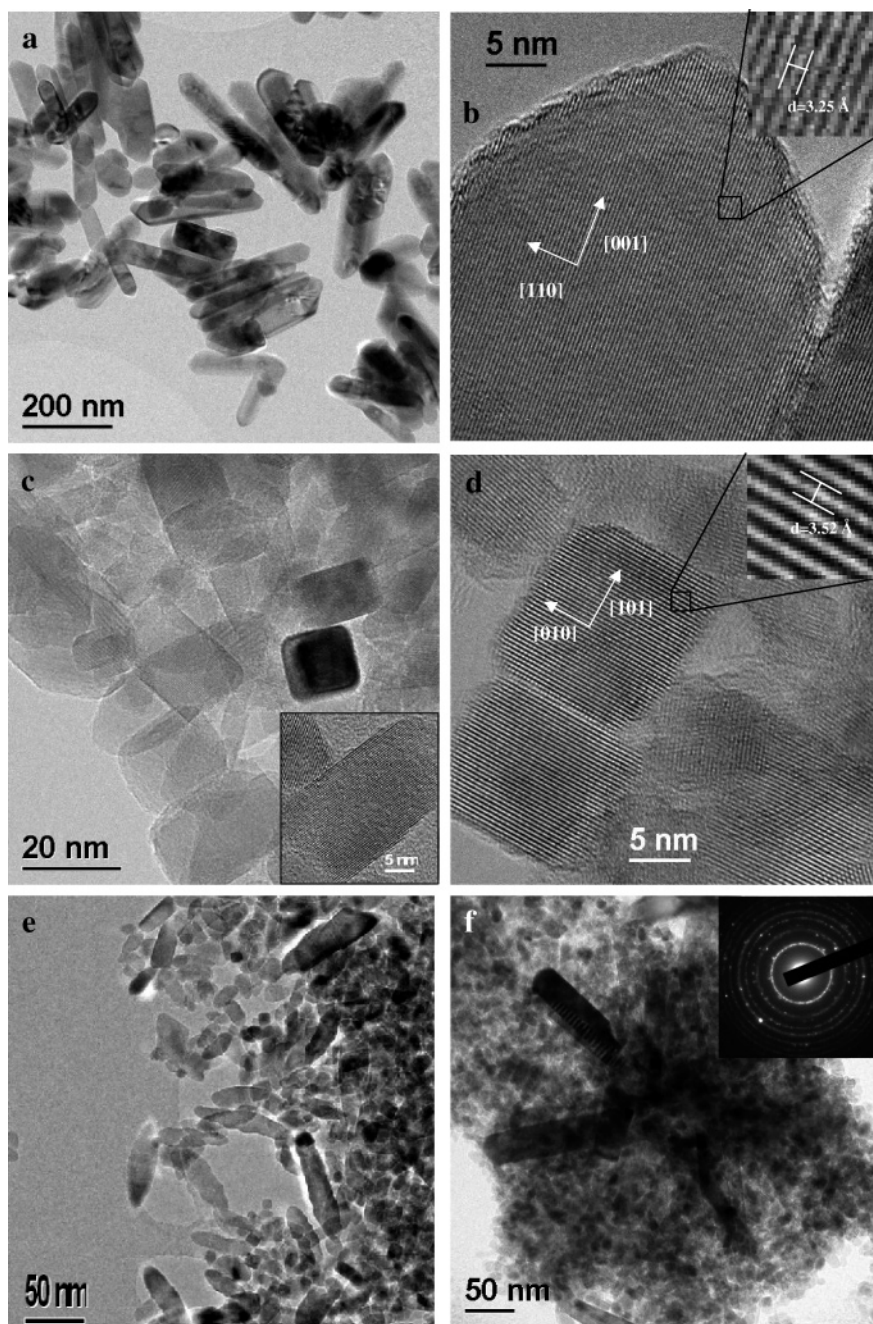


Figure 3. TEM (a,c,e,f) and HRTEM images (b,d). (a,b) Sample S371H, pure R. (c,d,e) Sample S22, pure A. (Inset c) HRTEM of an elongated A particle. (f) Sample S17, 52% A, 48% R. (Inset f) ED pattern; rings correspond to A, bright spots were indexed according to R.

the sample, as shown by the example of A and R mixture in Figure 3f. Brookite was identified by HRTEM analysis through selection of the electrons diffracted by the (211) planes. The crystallites present morphology similar to that of A and are hardly distinguishable in the TEM images.

4.1.2. The Effect of the Volume of Ammonia Solution, V_A , on the phase composition and crystallite size, was investigated at $T_R = 220$ and 161 °C (Figures 5 and 6) with $t_R = 2$ h. At 220 °C (Figure 5) the amount of A increases from 50 to 70% in the interval $V_A = 0$ –11 mL, and then it decreases progressively to zero after addition of 25–30 mL of ammonia solution. The fraction of A increases again on further addition of ammonia and attains 100% for $V_A > 44$ mL. Since A and R practically were the major phases observed for $V_A \leq 30$ mL, A and R present opposite trends. The fraction of brookite (B) shows a

maximum ($\sim 40\%$) close to the equivalence point at $V_A \approx 42$ mL, whereas it is of the order of the XRD detection limit⁴⁹ (3%) and even less for acidic and basic pH values. The crystallite size L_{XRD} of R increases from ~ 25 to ~ 80 nm with increasing V_A , while for A and B it decreases from 16 to 10 nm (Figure 5). At $T_R = 161$ °C (Figure 6) the fraction of both A and R progressively drops with increasing V_A , whereas the fraction of B increases. In any case, R is a minority phase (10–20%). Crystallite sizes have almost constant values of 10 nm for A and B and 22 nm for R.

4.1.3. The Effect of the Reaction Temperature, T_R , on the phase composition and particle size was studied in the range 110 – 250 °C for $t_R = 2$ h and $V_A = 20$ mL (Figure 7). Up to

(49) Li, G.; Li, L.; Boerio-Goates, J.; Woodfield, B. F. *J. Am. Chem. Soc.* **2005**, *127*, 8659.

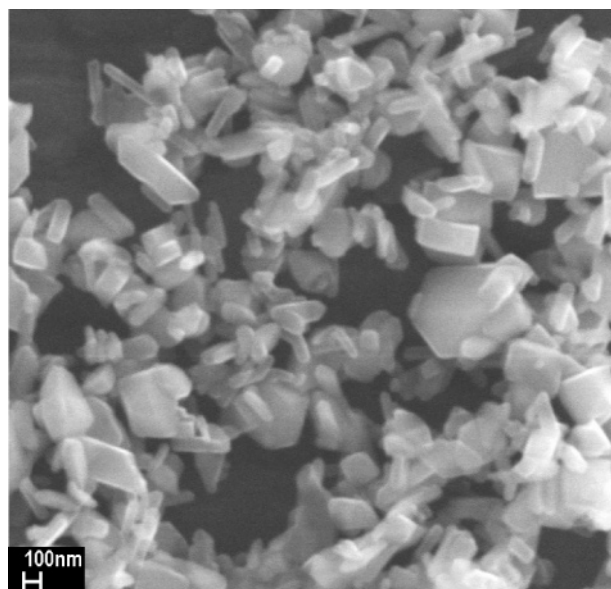


Figure 4. SEM image of sample S16, pure R.

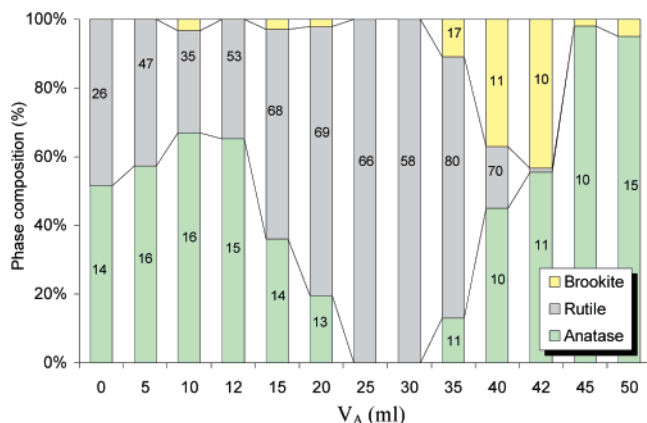


Figure 5. Phase composition (columns) and XRD crystallite size (numbers inside the columns, (nm)) of TiO_2 samples prepared at 220 °C with an aging time of 2 h. Numbers at the bottom of the columns represent the volume of ammonia solution.

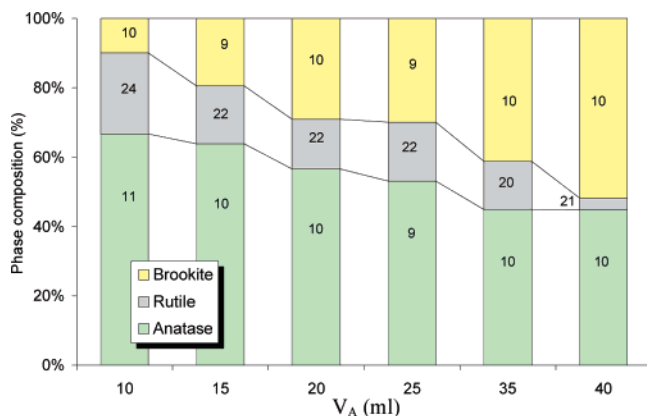


Figure 6. Phase composition (columns) and XRD crystallite size (numbers inside the columns, (nm)) of TiO_2 samples prepared at 161 °C with an aging time of 2 h. Numbers at the bottom of the columns represent the volume of ammonia solution.

160 °C phase composition and crystallite size remain almost constant. For $T_R > 160$ °C the amount of R progressively increases, as expected for acidic pH. B disappears at ~ 220 °C, and only traces of A are observed at ~ 250 °C. The evolution

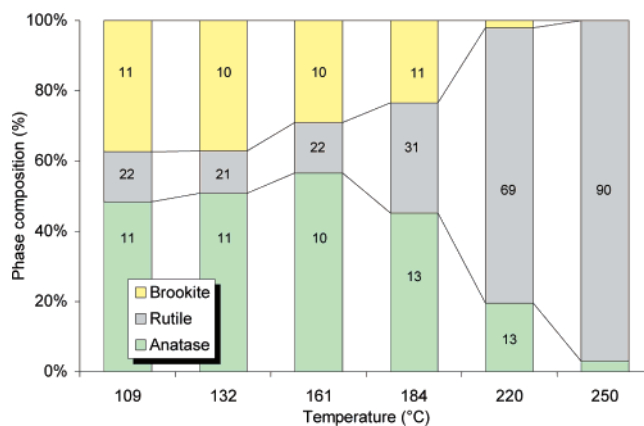


Figure 7. Phase composition (columns) and XRD crystallite size (numbers inside the columns, (nm)) of TiO_2 samples prepared with an aging time of 2 h after addition of 20 mL of ammonia solution. Numbers at the bottom of the columns represent the temperature.

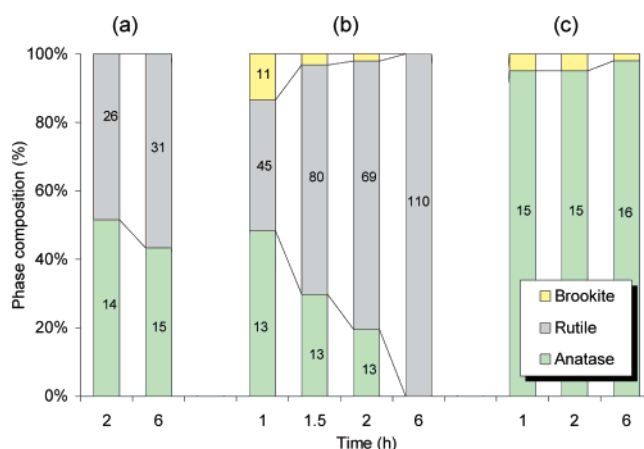


Figure 8. Phase composition (columns) and XRD crystallite size (numbers inside the columns, (nm)) of TiO_2 samples prepared at 220 °C for different aging times and (a) $V_A = 0$ mL, (b) $V_A = 20$ mL, (c) $V_A = 50$ mL. Numbers at the bottom of the columns represent the reaction time.

of phase composition is accompanied by the progressive increase of the crystallite size of R from 22 to 90 nm, while for A and B, L_{XRD} values are reasonably constant.

4.1.4. The Effect of the Aging Time, t_R , on the phase composition and particle size was investigated by varying the duration of the hydrothermal treatment in the range 1–6 h (Figure 8) for $T_R = 220$ °C and $V_A = 20$ mL. Moreover, a few syntheses were carried out for 1, 2, and 6 h using 0 and 50 mL of NH_3 solution, in order to study the combined effects of ammonia content and aging time. For $V_A = 20$ mL, the increase of t_R produces a progressive increase of the R fraction, and a decrease of the percentage of both A and B phases. The crystallites of R grow from 45 to 110 nm. For $V_A = 0$ mL the phase composition corresponds to a A/R ratio close to 1 and changes slowly with time. The crystallite size is ~ 30 nm for R and ~ 15 nm for A. At basic pH ($V_A = 50$ mL) the product is practically pure ($>98\%$) A with a constant crystallite size of ~ 15 nm.

4.1.5. Specific Surface Area and Porosity. The specific surface areas (A_{BET}) of selected samples are reported in Table S2 (Supporting information). The equivalent particle diameter (for spherical particles) or the mean edge length (for cubic particles), L_{BET} , can be calculated from A_{BET} by the equation

$$A_{\text{BET}} = \frac{6}{\rho L_{\text{BET}}} \quad (1)$$

As both rutile and anatase nanocrystals can be approximated as prismatic square-base particles with dimensions L_{BET} , L_{BET} , αL_{BET} (Figure 3), eq 1 becomes

$$A_{\text{BET}} = \frac{2(1 + 2\alpha)}{\alpha} \frac{1}{\rho L_{\text{BET}}} \quad (2)$$

where α can be evaluated from the TEM images (average value for 50–100 particles). The same equation can be used to estimate the expected surface area, A_{XRD} , from L_{XRD} , again assuming square-base prismatic crystals with dimensions L_{XRD} , L_{XRD} , αL_{XRD} and considering the weight fraction of each phase. A_{XRD} and A_{BET} agree within 10% error (Table S2). This is an indication that most of the surface of the TiO_2 particles is available for N_2 adsorption, i.e., there is only a small fraction of compact aggregates (Figure 3); the prismatic shape assumed for the particles is approximately correct. No evidence of the presence of amorphous titania was found for any of the samples.

TiO_2 powders with $L_{\text{BET}} < 50$ nm were mesoporous and show the typical nitrogen physisorption behavior matching that of the type-4 Brunauer⁵⁰ isotherm (see Figure S4, Supporting Information, as an example). It can be concluded that the measured porosity ($0.35\text{--}0.60$ mL g^{-1}) mainly corresponds to the voids between the packed particles, as revealed by the higher pore volumes—and smaller mean pore size—measured for the smaller particles (Table S2).

The thermal treatment at 400°C for 2 h in air had negligible effects on surface area, pore size distribution, and crystallite size.

4.1.6. Band Gap. The Kubelka–Munk function, $F(r) = (1 - r)^2/(2r)$, was used to calculate the optical absorbance from the relative reflectance (r) of the samples compared to the standard. The direct band gap was estimated from the Tauc plot^{51,52} of the quantity $(F(r) \cdot E)^{1/2}$ against the radiation energy, E , (Figure S5, Supporting Information) and corresponds to the intercept of the extrapolated linear portion of the plot with the energy axis. Pure A samples show a mean band gap of 3.13 ± 0.02 eV, while for pure R samples the band gap was 2.98 ± 0.02 eV, both in agreement with the literature values.¹² Degussa P25 gave the value of 3.02 ± 0.01 eV. Samples containing B, such as S13, have a band gap of 3.04 ± 0.01 eV. All samples with a significant R fraction have a band gap corresponding to that of pure rutile. The influence of particle size, washing treatment, and thermal annealing on band gap was negligible, at least for the conditions examined in the present work.

4.2. Photocatalytic Activity. The photocatalytic performance was evaluated by fitting the experimental data (TOC vs time) with the function

$$\text{TOC}(t) = C_0 - A \int_0^\infty \exp\left(-\frac{(t - t_0)^2}{s}\right) dt \quad (3)$$

where C_0 , A , t_0 , and s are the fitting parameters. Figure 9 shows

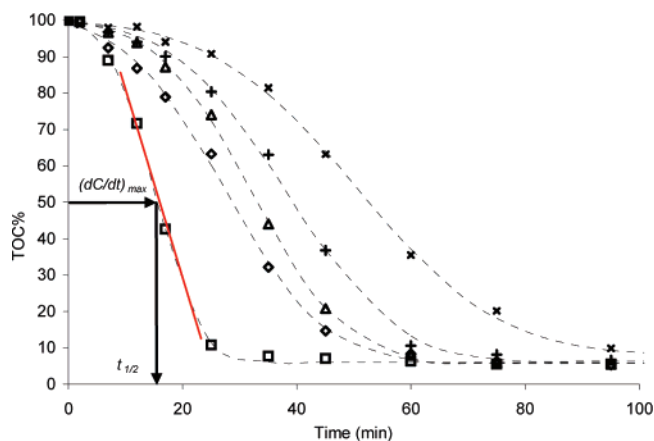


Figure 9. Mineralization curves of phenol (TOC %) of some representative samples (\square : S371H; \diamond : S18T; \triangle : Degussa P25; $+$: S12T; \times : blank). The dashed lines are the best fit to experimental data according to eq 5. The tangent straight line corresponds to the maximum mineralization rate $((dC/dt)_{\text{max}})$. The arrows indicate the half-transformation time ($t_{1/2}$). Kinetic data are normalized to the same mass of TiO_2 (100 mg).

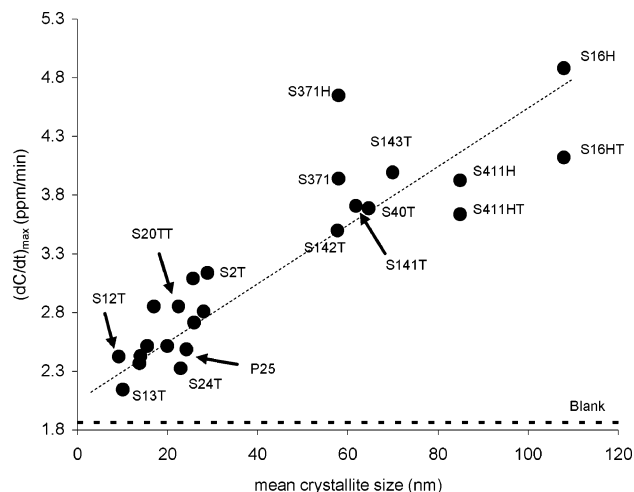


Figure 10. Maximum mineralization rate against mean crystallite size. The labels denote some significant samples. The horizontal dotted line indicates the blank. For multiphase samples, the mean crystallite size was calculated as weighted average of the mean size of the different polymorphs. The values of the maximum mineralization rate are normalized to the same mass of TiO_2 (100 mg).

the mineralization curves for some representative samples and the reference experiments (blank and P25).

The maximum mineralization rate, $(dC/dt)_{\text{max}}$, and the half-transformation time, $t_{1/2}$, calculated from eq 3 were taken as representative parameters to compare the mineralization kinetics of the different samples (Table S3, Supporting Information). The $(dC/dt)_{\text{max}}$ and $t_{1/2}$ values were normalized to the same mass (100 mg) of TiO_2 . The *relative mineralization rate* was calculated by assuming a nil value for the blank and a unity value for P25. As expected, $t_{1/2}$ decreases with increasing the maximum degradation rate.

The influence of phase composition and particle size was studied in detail. It was observed that (i) an increase of the R fraction and/or (ii) an increase of the particle size lead to an increase of activity (Figure 10). Moreover, many samples have $(dC/dt)_{\text{max}}$ higher than that measured for Degussa P25 photocatalyst. It is worth noting that conditions (i) and (ii) are not mutually independent: increasing the rutile fraction, the mean crystallite size—calculated taking into account the weight

(50) Brunauer, S.; Deming, L. S.; Deming, W. S.; Teller, E. *J. Am. Chem. Soc.* **1940**, *62*, 1723.

(51) Tauc, J.; Grigorovici, R.; Vancu, A. *Phys. Status Solidi* **1966**, *15*, 627.

(52) Serpone, N.; Lawless, D.; Khairutdinov, R. *J. Phys. Chem.* **1995**, *99*, 16646.

fraction of each phase—increases, because of the growing contribution of the bigger R crystallites with respect to A and B crystallites (Table S3). In our experimental conditions, a relatively high mineralization rate was observed even in blank tests (without TiO_2) due to the decomposition of H_2O_2 in hydroxyl radicals OH^\bullet under UV irradiation. Samples containing B, such as S13T, showed a lower photocatalytic activity with respect to pure A or R samples. The decrease of the surface area resulting from crystal growth does not produce a decrease of photocatalytic activity, indicating that the photodegradation process is not surface limited. For this reason the reactivity data were not normalized by the sample surface.

Some samples were prepared by avoiding the washing with ammonia solution (i.e., washing only with water and acetone) and/or annealing in order to preliminarily examine the influence of these processing parameters on the photocatalytic activity. It was observed that (iii) annealing of the powder lowers the catalytic activity for R samples, whereas the activity of A samples is enhanced; (iv) washing with the ammonia solution has a detrimental effect on the catalytic activity, in particular for R samples. The best performances were obtained for samples S371H and S16H, consisting of pure rutile with L_{XRD} of 58 and 108 nm, respectively. They present a relative mineralization rate of 3.3–3.5 (Table S3). Half-transformation of the organic substrate is obtained in a time corresponding to 65–70% of the time required for P25 and 32–34% of the time required for the blank. It has to be observed that the particles of S16H show a lower mean aspect ratio (3 instead of 5) and a broader particle size distribution with respect to S371H (compare Figures 3 and 4), as a result of the longer hydrothermal treatment (6 h instead of 2 h).

5. Discussion

The discussion of the results reported in the present paper has a two-fold objective: (i) to provide a rationale for explaining the evolution of phase composition and particle size during the hydrothermal synthesis of TiO_2 as a function of T_{R} , V_{A} , and t_{R} , and (ii) to understand the correlations between powder properties and photocatalytic activity.

(i) Evolution of Phase Composition and Particle Size. The evolution of the polymorph composition as obtained in the present study as a function of the different experimental variables (Figures 5–8) does not conform to the conventional explanation given in the literature. The TiO_2 formation mechanism is generally discussed on the basis of the partial charge model.^{3,18,24,53} According to this approach, solid polymorphs are thought to form by condensation of octahedral $[\text{Ti}(\text{OH})_6(\text{H}_2\text{O})_y]^{n+}$ units in the precursor solution, and the relative amount of each phase varies with the acidity of the aqueous solution because the pH determines the nature of the prevalent octahedral species. A decrease of acidity (high pH) determines an increase of the number of OH coordinated to Ti(IV) centers; consequently, the probability of edge-shared bonding is high, this favoring the A phase. Opposite, at low pH values, the number of OH ligands is low; as the edge-shared bonding requires that two condensations between pairs of Ti(IV) centers take place simultaneously, the corner-shared bonding may easily occur, favoring the R phase. In contrast, the present results (Figures

5–8) show that, at acidic pH, rutile is always the minor phase in the range 85–160 °C, whereas there is a nonmonotonic variation of the rutile fraction at 220 °C with increasing pH, and A prevails for $V_{\text{A}} = 5$ –12 mL. Only at alkaline pH was the predominant phase always anatase. It should be concluded that the partial charge model is not exhaustive in describing the hydrothermal synthesis of titania, at least, at acidic pH.

On the basis of the experimental results, we propose that the evolution of phase composition during hydrothermal synthesis of TiO_2 in acidic condition is a dynamic process which occurs under the influence of the different thermodynamic and kinetic factors, from small A to bigger R particles. Initially, during the heating of the autoclave, massive precipitation of nanocrystalline anatase occurs when the temperature exceeds 85 °C (size <5 nm after 10 min). At higher temperature and for relatively longer time (<1 h), anatase grows rapidly, from the initial size to a final size of 10–16 nm. In acidic conditions, the final size decreases with increasing pH. (Table S2). Accordingly, (i) Zhang and Banfield^{35,36} have provided convincing evidence that A is the stable phase when the particle size is smaller than 11–16 nm (critical size) because of its lower surface energy with respect to R (for bigger size, phase transformation from A to R can occur spontaneously); (ii) as indicated by the first-principles calculations of Barnard and Curtiss,⁴⁰ the critical size decreases with decreasing the surface acidity.

During the hydrothermal treatment, R particles grow significantly with time and temperature (from ~20 to ~100 nm, Figures 7, 8). On the contrary, the crystallite size of A (and B) does not change appreciably until complete disappearance of the phase. This evidence agrees with a growth mechanism mediated by aggregation of primary nanocrystals.^{4,14} Penn et al.^{54,56} gave evidence of the oriented aggregation of A nanocrystals in hydrothermal conditions. Barbè et al.⁵ showed that hindering the aggregation of A particles, the formation of R is suppressed. The aggregation of anatase nanocrystals in a highly oriented fashion with formation of elongated particles is supported by the TEM micrographs (Figure 3d,e). Once the critical size is exceeded, spontaneous transformation to rutile crystals with high aspect ratio, can take place. The rutile particles then develop facets and grow further from residual supersaturation or by Ostwald ripening.⁵³ A similar two-step growth mechanism has been reported by Zhang and Banfield for the precipitation of ZnS nanoparticles.⁵⁷

On the basis of the foregoing discussion, the evolution of phase composition and particles size during the hydrothermal treatment is controlled by two driving forces which act simultaneously: the phase transformation from anatase to thermodynamically more stable rutile crystals when the particle size exceeds a critical size (11–16 nm) and the reduction of the solid–liquid interface and thus overall (free energy) by crystal growth. Growth and, consequently phase composition, are mediated by mass transport, and the rate-determining step can be the transport process (diffusional or convective), the incorporation of new building units on the surface of the growing crystal, and the dissolution of the smaller particles (Ostwald ripening). Therefore, at strongly acidic pH, the observed

(53) Yin, S.; Hasegawa, H.; Maeda, D.; Ishitsuka, M.; Sato, T. *J. Photochem. Photobiol., A* **2004**, *163*, 1.

(54) Penn, R. L.; Oskam, G.; Strathmann, T. J.; Searson, P. C.; Stone, A. T.; Veblen, D. R. *J. Phys. Chem. B* **2001**, *105*, 2177.

(55) Penn, R. L.; Banfield, J. F. *Science* **1998**, *281*, 969.

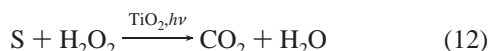
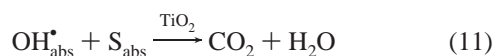
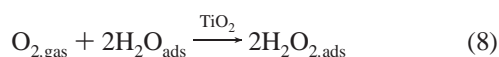
(56) Penn, R. L.; Banfield, J. F. *Geochim. Cosmochim. Acta* **1999**, *63*, 1549.

(57) Huang, F.; Zhang, H.; Banfield, J. F. *Nanoletters* **2003**, *3*, 373.

evolution of size and phase distribution may depend (i) on the overall concentration of aqueous titanium species (solubility), (ii) on the specific species involved in the formation of new building units, and (iii) on the species which are adsorbed at the surface and have to be desorbed/removed when a new building unit is added.

The thermodynamic calculations do not show any sudden variation of pH (Figure S1, Supporting Information) or TiO₂ solubility (Figures S2, S3, Supporting Information) with temperature or volume of ammonia solution in relation with the observed changes of phase composition. On the contrary, when the stability diagrams (Figure 1) are compared with the evolution of phase composition (Figures 5–7), some interesting trends can be found. At 220 °C, the first minimum of the rutile fraction (30% rutile, V_A = 10–12 mL) corresponds well with the boundary (pH = 0.2) between the Ti(OH)³⁺ and Ti(OH)₂²⁺ predominance regions, while the maximum (100% rutile, V_A = 25–30 mL) lies on the boundary (pH = 0.6) between the Ti(OH)₂²⁺ and the Ti(OH)₄ predominance regions (Figure 1c). Below 180 °C, Ti(OH)₂²⁺ is the only predominant aqueous species at acidic pH (V_A < 42 mL). A monotonous decrease of both A (major phase) and R fraction, and hence an increase of B fraction up to 50%, was observed at 160 °C (Figure 6). It is possible that, at this relatively low temperature, the transformation of A to R is rather slow and is mediated by the formation of brookite. For T > 180 °C (Figure 7) rutile coarsening is fast. This suggests that the rate-controlling process could be an activated process as the incorporation of new building units by surface reaction or nucleation of new steps on the flat crystal surface. Thus, it is plausible to suppose that the nature of the building units or the species that are adsorbed onto the surface (e.g., Ti(OH)₂²⁺ for R and Ti(OH)₄ for A) are related to the prevalent species in solution, and this relationship is the reason of the correspondence depicted in Figure 1c.

(ii) Photocatalytic Activity. A general simplified scheme of the photomineralization process of an organic substrate is given by eqs 4–11 where S indicates the organic substrate. Equation 12 schematizes the whole process.⁵⁸



Only photons with energy equal to or higher than that of the semiconductor band gap (E_g), are able to promote the formation of electron–hole (e^- , h^+) pairs (eq 4). Charge carriers can be

trapped as Ti³⁺ and O[•] defect sites in the TiO₂ lattice, or recombine (eq 5), with energy dissipation. Both electron and hole may, in principle, react and generate •OH radicals adsorbed at the surface (eqs 6, 7). Two •OH radicals may be apparently produced per adsorbed photon. However, by considering the competition between reactions expressed by eq 7 and eqs 9–10, the production of •OH radicals by e^- (eq 7) should be strongly inhibited.⁵⁹ Hydroxyl radicals, due to their high oxidizing potential⁵⁸ (2.80 V), react with the majority of the organic substrates (S), till complete mineralization (eq 11). Hydrogen peroxide reactant in eq 7, can be directly supplied to the system or produced from gaseous oxygen (eq 8).

The experimental kinetic data are related only to the overall process (eq 12), i.e. to the disappearance of the organic carbon, and no other intermediate chemical species followed. Nevertheless, a limited number of stages can be identified and discussed. The whole process (eq 12) is promoted if: (i) the organic molecules S, (ii) H₂O₂, and (iii) OH[•] are efficiently adsorbed on the surface, (iv) H₂O₂ and (v) electron–hole pairs are efficiently produced on the surface, and (vi) electron–hole recombination is inhibited. Each stage may give a significant contribution to the whole process (eq 12), but some speculation on their relative importance can be formulated.

First, the stages related to H₂O₂ (iv) and electron–hole pairs (v) production, have minor relevance. In fact hydrogen peroxide was used as reactant in photodegradation experiments and its production from gaseous oxygen is not strictly required (eq 8). The electron–hole pairs production depends on the irradiation intensity and on the E_g value. As the irradiation conditions were unchanged in the photodegradation experiments, differences in the electron–hole pairs production among different samples should be ascribed to different E_g values. However, the small difference between band gaps of pure titania samples (<5%) should not exert any significant influence on the photocatalytic activity.^{17,52,60}

Second, the adsorption stages (i–iii) are expected to be strongly affected by pH and ionic strength as well as different organic substrates S—and their intermediate degradation products—can be differently adsorbed on the titania surface. In the present paper, all the photocatalytic tests were performed with the same kind and amount of substrate (phenol) and electron acceptor (H₂O₂), maintaining pH and ionic strength unchanged. Consequently, the ability of the different species to chemisorb on the surface (i–iii) can be only attributed to the nature of the surface itself. Besides, for a given crystalline phase, each crystallographic surface exposed to the solution/irradiation may present different adsorption proprieties.^{10,61–62}

Third, electron–hole recombination (vi) is often considered of primary relevance.^{14,17,60,63–65} Recombination may occur on

(58) Sclafani, A. J. *Phys. Chem.* **1996**, *100*, 13655.

(59) Bellobono, I. R.; de Martini, G.; Tozzi, P. M.; Canevali, C.; Morazzoni, F.; Scotti, R.; Bianchi, R. *Int. J. Photoeng.* **2006**, *8*, no. 26870.

(60) Riegel, G.; Bolton, J. R. *J. Phys. Chem.* **1995**, *99*, 4215.

(61) Morris Hotsenpiller, P. A.; Bolt, J. D.; Farneth, W. E. *J. Phys. Chem. B* **1998**, *102*, 3216.

(62) (a) Ohno, T.; Sarukawa, K.; Matsumura, M. *New J. Chem.* **2002**, *26*, 1167. (b) Taguchi, T.; Saito, Y.; Sarukawa, K.; Ohno, T.; Matsumura, M. *New J. Chem.* **2003**, *27*, 1304.

(63) Du, Y.; Rabani, J. *J. Phys. Chem. B* **2003**, *107*, 11970.

(64) Emilio, C. A.; Litter, M. I.; Kunst, M.; Bouchard, M.; Colbeau-Justin, C. *Langmuir* **2006**, *22*, 3606.

(65) Kominami, H.; Kato, J.-i.; Muratami, S.-y.; Ishii, Y. a.; Kohno, M.; Yabutani, K.-I.; Yamamoto, T.; Kera, Y.; Inoue, M.; Inui, T.; Ohtani, B. *Catal. Today* **2003**, *84*, 181.

the surface or in the bulk and is in general catalyzed by impurities, defects, or all factors which introduce bulk or surface imperfections into the crystal.⁶⁴ According to these arguments, well-crystallized faceted particles showed enhanced photoactivity with respect to powders with poorly crystalline surface^{3,14,46,53,62,65–67} and the photoreactivity increased with the crystallite size,^{14,17,66,68} the surface itself being an intrinsic defect.

As a result of these considerations, stage (vi) (recombination) and stages (i–iii) (adsorption), associated to the surface properties of the solid, may be considered of primary relevance in determining the rate of phenol photodegradation and may be suitably related to the phase composition, crystallite size, and particle morphology of the powders.

Inspection of Figure 10 reveals that the general linear trend includes most of the samples, independently of their phase composition. This suggests that the property mainly influencing the photocatalytic behavior is the crystallite size and that the reasons of the higher photocatalytic activity of R samples, with respect to A, are related to the larger size and higher aspect ratio of rutile particles (as discussed later). Photochemistry similar for A and R was reported^{14,17,58,63,69,70} when particles with the same size and morphology are compared. In particular, Sclafani and co-workers⁵⁸ ascribed the often reported reason of the higher reactivity of A with respect to R to its higher O₂ exchange ability, while in the presence of different electron acceptor species, such as H₂O₂, R has revealed a significant catalytic activity, comparable to that of anatase.

All TiO₂ powders investigated in the present study are well crystallized and well faceted as a consequence of the coarsening and ripening processes occurring under hydrothermal conditions. Indications of the absence of low-density phases, amorphous surface layers, high concentration of lattice hydroxyl groups and closed porosity are provided by the good agreement between the measured and calculated density as well as by the correspondence of the values of L_{XRD} , L_{BET} , and L_{TEM} (Table S2). Therefore, the particles can be considered to contain a relatively low concentration of defects, both in the bulk and on the surface. The larger the crystal size, the smaller is the specific surface area with a further decrease of the number of intrinsic surface defects, resulting in a lower recombination rate, which explains the general trend shown in Figure 10.

It was reported that oxidation and reduction sites on the R particles occur on the {011} and the {110} faces, respectively, while, for A particles, the oxidation sites are mainly on the {001} faces, and the reduction sites are mainly on the {011} faces.⁶² Therefore, the presence of well-developed faces on TiO₂ particles is advantageous for providing both oxidation and reduction sites. Moreover, it is expected that the efficiency of electron–hole separation is enhanced because of the difference in the electronic band structure between different crystals surfaces. This suggests that R, which has higher aspect ratio than A and larger surfaces, should present higher spatial separation between oxidation and reduction sites with lower probability of recombination.

Modifications of the surface chemistry of the powders induced by changing the washing treatment (exclusion of the ammonia washing) or thermal annealing were found to have a notable effect on the photocatalytic properties. Ammonia washing (samples S37I and S37IH) and calcination at 400 °C for 2 h (samples S16H and S16HT; S41IH and S41IHT) resulted in a decrease of performance. Both effects can be attributed to a decreasing number of the surface acidic sites and the direct influence of these sites on the absorption stages (i–iii). A prolonged thermal treatment (10 h) at higher temperature (550 °C) performed to increase the particle size of anatase (from 9.5–22.5 nm) resulted in an improvement of the photocatalytic activity. This indicates that the beneficial effect of coarsening overcomes the detrimental effect of the thermal treatment itself (samples S12T and S20TT, Figure 10, Table S2). In agreement with our results, the increase of the number of surface acidic sites was cited as a reason of improved performance.¹⁷ It is well-known that their concentration can be modified by washing⁷ or by thermal treatments.^{66,71} The above considerations suggest that the overall efficiency of the photocatalytic degradation process is determined by the combined effect of stages (vi) and (i–iii).

6. Summary and Conclusions

A systematic approach was applied to the hydrothermal synthesis of TiO₂ nanoparticles to gain insight into the fundamental factors controlling phase composition, particle size, crystal morphology, and photocatalytic activity.

Phase-stability diagrams were generated using a thermodynamic model of the TiO₂–H₂O–HCl–NH₃ system to understand which aqueous titanium species in equilibrium with solid titania predominate as a function of pH, temperature, and reactant concentration. The solubility of the solid phase was calculated as a function of the above chemophysical variables. TiO₂ nanoparticles were prepared using a TiOCl₂ solution with concentration of 0.45 mol/kg by hydrothermal synthesis at different temperatures in the range 85–250 °C, mainly at 160 and 220 °C. Control of the phase composition and particle size was attained by changing the temperature of hydrothermal treatment, the pH (by addition of volumes of ammonia solution), and the reaction time. Repetition of the same experiment indicated that the reproducibility of phase composition was within ± 5 wt %. During heating up, massive precipitation of nanocrystalline anatase with particle size of ~ 5 nm occurs when the temperature exceeds 85 °C. As the temperature increases further, this initially precipitated solid phase undergoes coarsening (from 5 to 10–16 nm) and then transformation in brookite and rutile. However, the evolution of phase composition is strongly dependent on final temperature, pH, and reaction time. Comparison with the thermodynamic stability diagrams suggests a correlation between the phase composition and the predominant aqueous titanium species in solution. At high temperature (180–250 °C) and strongly acidic pH, formation of rutile from preexisting anatase is associated to Ti(OH)₂²⁺ and Ti(OH)³⁺ as predominant ions. At pH > 0.5, Ti(OH)₄ becomes the predominant aqueous species, and the formation of rutile is slowed down. At basic pH, anatase is the exclusive hydrothermal product. Below 180 °C, the predominant titanium species in acidic environment is always Ti(OH)₂²⁺. In these conditions,

(66) Cho, C. H.; Kim, D. K. *J. Am. Ceram. Soc.* **2003**, *86*, 1138.

(67) Wahli, R. K.; Yu, W. W.; Liu, Y.; Mejia, M. L.; Falkner, J. C.; Nolte, W.; Colvin, V. L. *J. Mol. Catal. A: Chem.* **2005**, *242*, 48.

(68) Grela, M. A.; Colussi, A. J. *Phys. Chem.* **1996**, *100*, 18214.

(69) Kiselev, A.; Andersson, M.; Mattson, A.; Shchukarev, A.; Sjöberg, S.; Palmqvist, A.; Österlund, L. *Surf. Sci.* **2005**, *584*, 98.

(70) Koelsch, M.; Cassaignon, S.; Ta Thanh Minh, C.; Guillemoles, J.-F.; Jolivet, J.-P. *Thin Solid Films* **2004**, *451–452*, 86.

(71) Bakardjieva, S.; Šubr, J.; Štengl, V.; Dianez, M. J.; Sayagues, M. J. *Appl. Catal., B* **2005**, *59*, 193.

the powders are mainly composed of anatase and brookite, whereas the rutile fraction is <20%. This suggests that the transformation of anatase to rutile is strongly slowed down at low temperature, with formation of brookite as intermediate phase.

As a consequence of the hydrothermal treatment, the TiO₂ powders are well-crystallized and well dispersed, without formation of large aggregates. The morphology of the rutile crystals corresponds to faceted and elongated prismatic particles with an aspect ratio (length/width) of ~5. The anatase particles have aspect ratios between 1 and 3. The particle size can be controlled by changing the experimental conditions and varies between 10 and 16 nm for anatase and 20–110 nm (width) for rutile. The size of the brookite nanocrystals is almost constant (10 nm). According to literature, transformation to rutile seems to occur when the anatase nanocrystals have attained a critical size which depends on the pH. Growth of anatase and transformation to rutile can be also mediated by oriented attachment of anatase nanocrystals along the [101] and other directions. Once transformation has occurred, the rutile crystals can grow further in the [001] direction.

Photocatalytic performance of the titania powders was evaluated by measuring the kinetics of phenol mineralization in the presence of H₂O₂ under UV irradiation. It turned out that the photocatalytic activity increases with increasing crystallite size. This suggests that the electron–hole pair recombination plays an important role during the photodegradation of phenol, at least under the present experimental conditions. Recombination is apparently slower in well-faceted and big rutile particles, thus promoting a higher activity, despite the decrease of specific surface area. Modification of the surface chemistry of the powders was also found to significantly affect the kinetics of the photomineralization process. Thermal annealing at 400 °C and washing with ammonia solution depress the photocatalytic activity probably because the concentration of acidic surface sites is decreased by these treatments. Therefore, the degradation rate (relative mineralization rate of 3.5), higher than that of the

most common reference material Degussa P25 observed for faceted, well-dispersed, and relatively big prismatic rutile crystals (width 50–100 nm, length 250–500 nm) results from the combination of three factors: (i) the increase of photocatalytic activity with increasing particle size and rutile content, (ii) the high aspect ratio of the rutile crystals, and (iii) a high concentration of acidic surface sites.

In conclusion, optimization of the photocatalytic properties of hydrothermal TiO₂ has been obtained through a systematic investigation of the influence of temperature, pH, and duration of the hydrothermal treatment on phase composition, particle size and shape, with the support of a thermodynamic model. As the large majority of the operative cost of an industrial photomineralization unit can be ascribed to the energy supplied to the UV source, an increase of the mineralization rate corresponds to a decrease of the operating costs, with a significant advantage coming from the use of a well-optimized photocatalyst powder. Moreover, the simple, low cost and reproducible synthesis process reported herein makes it of potential interest for industrial exploitation.

Acknowledgment. We thank the Cariplo Foundation for financial support, and Mr. C. Bottino and Mrs. M. Bassoli (IENI-CNR) for their contribution to the sample characterizations.

Supporting Information Available: Chemical species considered in the thermodynamic calculations are reported in Scheme S1 and the corresponding reference thermochemical data in Table S1; preparation conditions and properties of all investigated titania samples are reported in Table S2; photocatalytic properties of titania samples are shown in Table S3; further results of thermodynamic calculations are reported in Figures S1–S3; typical nitrogen physisorption isotherm is reported in Figure S4; Tauc plot of some representative samples for band gap calculation is shown Figure S5. This material is available free of charge via the Internet at <http://pubs.acs.org>.

JA067050+

Supporting Information

Optimizing the photocatalytic properties of hydrothermal TiO₂ by the control of phase composition and particle morphology. A systematic approach.

**Andrea Testino^{a*}, Ignazio Renato Bellobono^b, Vincenzo Buscaglia^c Carmen Canevali^a,
Massimiliano D'Arienzo^a, Stefano Polizzi^d, Roberto Scotti^a, and Franca Morazzoni^a**

^a Department of Materials Science, University of Milano-Bicocca, Via R. Cozzi 53, I-20125 Milano, Italy

^b Department of Physical Chemistry, Environmental Research Centre, University of Milano, Via Golgi 19, I-20133 Milano, Italy

^c Institute for Energetics and Interphases, Dept. of Genova, National Research Council, Via De Marini, 6, I-16149, Genova, Italy

^d Department of Physical Chemistry, University of Venezia, Via Torino 155/b, I-30172 Venezia, Italy

* Corresponding author. E-mail: andrea.testino@mater.unimib.it

Contents

Scheme S1. Chemical equilibria considered in the thermodynamic calculations of the TiO₂-H₂O-HCl-NH₃ system.

Table S1. Thermochemical properties of chemical species in the TiO₂-H₂O-HCl-NH₃ system.

Table S2. Properties of hydrothermal TiO₂ powders.

Table S3. Photocatalytic properties of selected TiO₂ powders.

Figure S1. pH of the TiOCl₂ solution as a function of temperature.

Figure S2. Solubility of TiO₂ as a function of temperature and ammonia solution volume.

Figure S3. Solubility of TiO₂ as a function of ammonia solution volume at two different temperatures.

Figure S4. Nitrogen adsorption/desorption isotherm of a mesoporous TiO₂ sample.

Figure S5. Tauc plot of some TiO₂ representative samples.

Scheme S1. Relevant equilibria in the $\text{TiO}_2\text{-H}_2\text{O-HCl-NH}_3$ system. In the reactions, the H_2O molecules are not reported as ligands in the Ti complexes. These have to be considered as octahedrally coordinated, e.g. $[\text{Ti}(\text{Cl})_3(\text{H}_2\text{O})_3]^+$ instead of TiCl_3^+ .

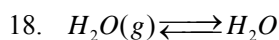
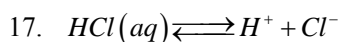
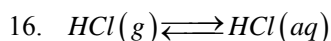
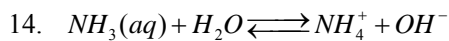
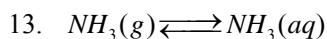
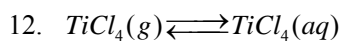
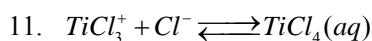
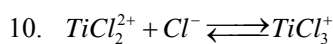
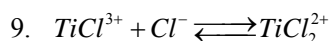
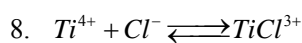
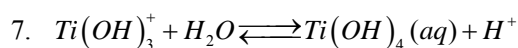
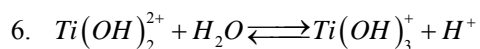
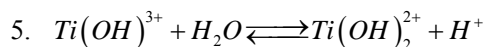
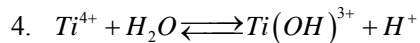
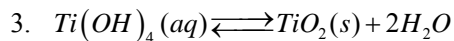
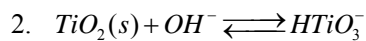
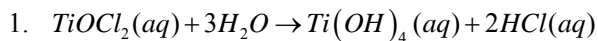


Table S1. Relevant species in the TiO₂-H₂O-HCl-NH₃ system and corresponding standard state properties at 298.15 K [36]

	Ionic species											
	H ⁺	OH ⁻	NH ₄ ⁺	Cl ⁻	Ti ⁴⁺	TiCl ³⁺	TiCl ₂ ²⁺	TiCl ₃ ⁺	TiOH ³⁺	Ti(OH) ₂ ²⁺	Ti(OH) ₃ ⁺	HTiO ₃ ⁻
ΔG° (J mol ⁻¹) 10 ⁻⁴	0	-15.7	-7.95	-13.1	-35.4	-44.5	-58.7	-72.7	-61.4	-87.0	-109	-95.6
ΔH° (J mol ⁻¹) 10 ⁻⁵	0	-2.30	-1.33	-1.67	-4.22	-5.58	-7.45	-9.47	-6.71	-9.52	-12.2	-10.4
S° (J mol ⁻¹ K ⁻¹) 10 ⁻¹	0	-1.07	11.1	5.67	-45.6	-43.5	-41.0	-43.9	-19.0	-4.08	5.69	11.7
$C^\circ p$ (J mol ⁻¹ K ⁻¹) 10 ⁻¹	0	-13.7	6.59	-12.3	98.7	54.9	108	157	-32.2	-105	-153	-10.6
V° 10 ⁶ (m ³ mol ⁻¹)	0	-4.18	18.1	17.8	-10.4	-38.0	-17.9	5.40	-6.52	-3.77	-1.51	-2.21

	Aqueous species					Gaseous species				Solid species
	H ₂ O	Ti(OH) ₄	NH ₃	TiCl ₄	HCl	HCl	H ₂ O	NH ₃	TiCl ₄	TiO ₂ (anatase)
ΔG° (J mol ⁻¹) 10 ⁻⁴	-23.7	-132	-2.67	-86.7	-9.51	-9.53	-22.9	-1.65	-72.6	-88.3
ΔH° (J mol ⁻¹) 10 ⁻⁴	-28.6	-151	-8.13	-117	-11.6	-9.23	-24.2	-4.61	-76.3	-93.9
S° (J mol ⁻¹ K ⁻¹) 10 ⁻¹	7.00	5.48	10.8	-53.6	10.5	18.7	18.9	19.2	35.3	4.99
$C^\circ p$ (J mol ⁻¹ K ⁻¹) 10 ⁻¹	7.53	5.02	7.49	201	-3.18	2.91	3.36	3.56	9.54	5.53
V° 10 ⁶ (m ³ mol ⁻¹)	18.1	-350	24.4	32.9	0	-	-	-	-	20.5
a (J mol ⁻¹ K ⁻¹)	-	-	-	-	-	-	-	-	-	69.9
b 10 ³ (J mol ⁻¹ K ⁻²)	-	-	-	-	-	-	-	-	-	8.54
c 10 ⁻⁵ (J mol ⁻¹ K)	-	-	-	-	-	-	-	-	-	-15.3

Table S2. Summary of hydrothermal synthesis experiments and properties of the corresponding titania powders.

Sample ⁽¹⁾	Synthesis conditions ⁽²⁾			Anatase			Rutile			Brookite			density		Specific surface		Pores
ID	V_A	t_R	T_R	Wt.	d (101)	$\alpha^{(3)}$	Wt.	d (110)	$\alpha^{(3)}$	Wt.	d (211)	$\alpha^{(3)}$	XRD ⁽⁴⁾	$\rho^{(5)}$	XRD ⁽⁶⁾	BET	BJH DPV ⁽⁷⁾
	(ml)	(h)	(°C)	%	(nm)	(-)	%	(nm)	(-)	%	(nm)	(-)	(g cm ⁻³)		(m ² g ⁻¹)		(ml g ⁻¹)
S0	0-50	0.17	85	>90	<5		<5	<5		<5	<5						
S2 [1]	5	2	220	57	15.8		43	47		-							
S3 [1]	12	2	220	65	14.6		35	53		-			4.01	3.89		68	0.41
S12 [1]	45	2	220	98	9.5		0	-		2	n.d.		3.81	3.76		129	0.59
S13 [1]	42	2	220	56	10.5		1	n.d.		43	10.0		4.00	3.91		88	0.51
S141 [3]	20	2	220	20	13.1	1	78	73	5	2	n.d.	1	4.18	4.05	45	46	
S142 [1]	20	1.5	220	30	12.7		67	80		3	10.7		4.14	4.08			
S143 [3]	20	2	161	57	9.9		14	22		29	10.0						
S15 [1]	20	1	220	48	12.5		38	46		13	16.7		4.02	3.97		71	0.34
S16 [1]	20	6	220	-	-	-	100	108	3	-			4.24	4.24	10	11	0.03 ⁽⁸⁾
S17 [1]	0	2	220	52	14.3	2	48	26	5	-		2	4.06	3.91	66	64	
S18 [2]	10	2	220	67	15.7	3	30	35	5	3	12.0	3	3.97	3.85	73	68	
S19 [1]	50	6	220	98	15.9		0	-		2	n.d.			3.81			
S20 ⁽⁹⁾ [1]	-	-	-	100	22.5		0	-		-				3.82			
S21 [1]	0	6	220	43	14.9		57	31		-				3.99			
S22 [1]	50	2	220	95	14.9	1	0	-		5	n.d.	1	3.90	3.80	98	91	
S23 [1]	50	1	220	95	14.6		0	-		5	n.d.			3.80			
S25 [1]	40	2	161	45	10.2		3	21		52	10.2			3.93			
S26 [1]	20	2	109	48	11.2		14	22		37	10.6			3.93			
S27 [1]	20	2	132	51	11.2		12	21		37	10.2		4.02	3.90		91	
S28 [1]	20	2	184	45	13.2		31	31		23	11.1			3.95			
S33 [1]	15	2	161	64	10.2		17	22		19	9.3						
S34 [1]	25	2	161	53	9.4		17	22		30	9.1						
S35 [1]	35	2	161	45	9.7		14	20		41	9.5						
S361 [1]	10	2	161	67	11.1		23	24		10	10.0		4.00	3.86		94	
S371 [2]	30	2	220	-	-	-	100	58	5	-			4.24	4.20	18	20	
S38 [1]	15	2	220	36	13.9		61	68		3	n.d.						
S40 [1]	25	2	220	-	-	-	100	66		-							
S411 [1]	20	2	250	3	n.d.		97	87		-							
S412 [2]	35	2	220	13	10.8	3	76	80	5	11	17.2	3			32		
S42 [1]	40	2	220	45	10.1	3	18	71	5	37	10.6	3	4.05	3.96		88	
P25	-	-	-	77	23		23	37.5		-						54	0.14

- (1) The number in square brackets is the number of repetitions of the experiments. The reported data in the arrow are the mean value.
- (2) V_A : volume of ammonia solution; t_R : reaction time; T_R : reaction temperature.
- (3) Aspect ratio, α =length/width, estimated from TEM images.
- (4) Density calculated from Rietveld refinement of the XRD patterns.
- (5) Experimental density from He pycnometry
- (6) Calculated from composition, crystallite size and α for each phase.
- (7) BJH Desorption Pore Volume
- (8) Non-mesoporous material (Type 2 isotherm)
- (9) Obtained treating sample S12 at 550°C for 10h

Table S3. Photocatalytic properties of selected titania samples.

Sample	$(dC/dt)_{max}^{(1)}$	$t_{1/2}^{(2)}$	Mean Crystallite size ⁽³⁾	Relative Mineralization Rate ⁽⁴⁾	Specific Surface Area
	(ppm/min)	(min)	(nm)	(-)	(m ² g ⁻¹)
Blank	1.81	55	-	0	-
Degussa P25	2.66	28	26	1	54
S2T	3.08	29	29	1.5	
S3T	2.76	35	28	1.1	68
S12T	2.37	39	9	0.7	129
S13T	2.09	43	10	0.3	88
S141T	3.66	24	62	2.2	46
S142T	3.45	25	58	1.9	
S15T	3.04	31	26	1.4	71
S16H	4.83	18	108	3.5	11
S16HT	4.07	21	108	2.6	11
S17T	2.46	39	20	0.8	64
S18T	2.80	33	17	1.2	68
S19T	2.46	41	16	0.8	
S20TT ⁽⁵⁾	2.80	33	23	1.2	
S21T	2.44	27	24	0.7	
S22T	2.38	40	14	0.7	91
S23T	2.32	43	14	0.6	
S24T	2.27	39	23	0.5	
S371H	4.60	19	58	3.3	20
S371	3.89	22	50	2.4	
S40T	3.94	23	70	2.5	
S411H	3.88	24	85	2.4	
S411HT	3.58	25	85	2.1	

(1) Calculated as shown in Figure 13. Standard error 0.2 ppm/min

(2) Calculated as shown in Figure 13. Standard error 3 min

(3) Calculated as weighted mean value of the crystallite size (XRD) of the different polymorphs.

(4) Calculated by setting 0 for blank and 1 for Degussa P25

(5) Obtained treating sample S12 at 550°C for 10h

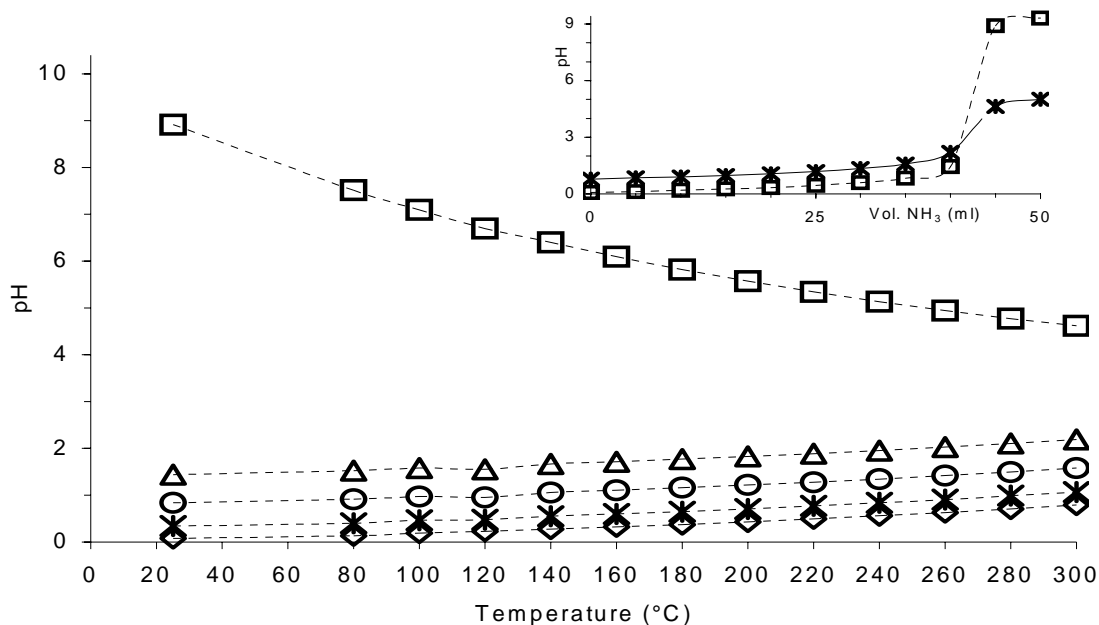


Figure S1. pH as a function of temperature under hydrothermal conditions calculated for an overall Ti concentration of 0.45 mol/kg and different ammonia solution volumes (□: 45 ml; △: 40 ml; ○: 35 ml; *: 20 ml; ◇: 0 ml). Inset: pH as a function of ammonia solution volume for different temperatures (□: 25 °C; *: 300 °C).

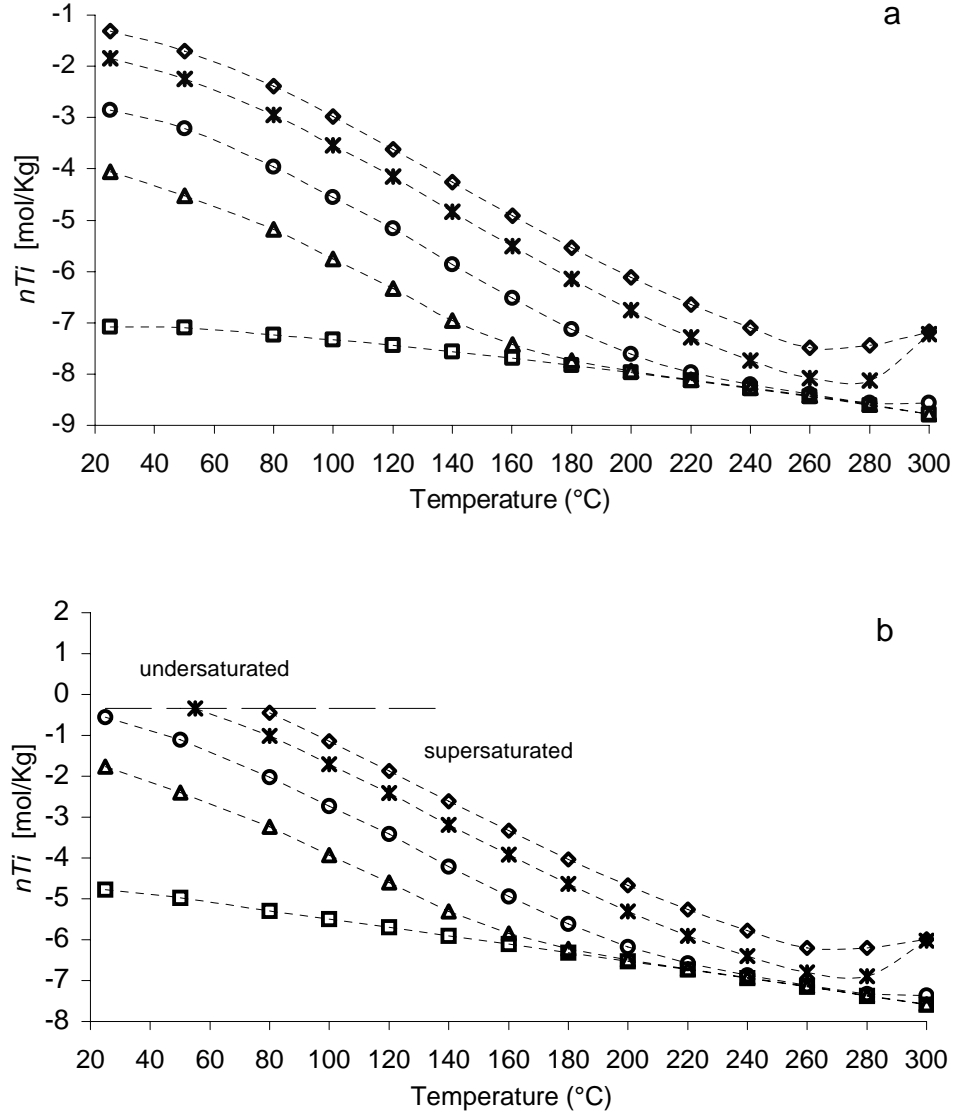


Figure S2. Solubility of TiO_2 as a function of temperature under hydrothermal conditions calculated for an overall Ti concentration of 0.45 mol/kg and different ammonia solution volume (□: 45 ml; △: 40 ml; ○: 35 ml; *: 20 ml; ◇: 0 ml). (a) Influence of particle size neglected. (b) Calculated for 12 nm particles ($\gamma = 0.5 \text{ J m}^{-2}$). The horizontal line in (b) denotes $n_{\text{Ti}} = 0.45 \text{ mol/Kg}$. The quantity n_{Ti} plotted on the y-axis represents the overall amount (mol/Kg) of titanium in solution and takes into account all the aqueous species. The solubility curves in Fig S2b were calculated using the Gibbs-Thompson equation

$$\ln \frac{K_{s,d}}{K_s} = 4 \frac{\nu \gamma_{l,s}}{k_B T d}$$

where K_s is the solubility constant of a macroscopic crystal, $K_{s,d}$ is the solubility constant of a crystal with diameter d , ν is the unit cell volume, γ is the liquid-solid surface energy, T the temperature and k_B

the Boltzmann constant. The dashed horizontal line in Fig. S2b corresponds to a concentration of 0.45 mol/kg. This line meets the curve $V_A = 0$ ml at $T \approx 80^\circ\text{C}$. Experimentally, it has been observed that a clear 0.45 mol/kg solution, when heated from room temperature to 100°C , produces a precipitation of anatase nanocrystals starting at $80\text{--}85^\circ\text{C}$ in 1-3 minutes, in agreement with the calculations

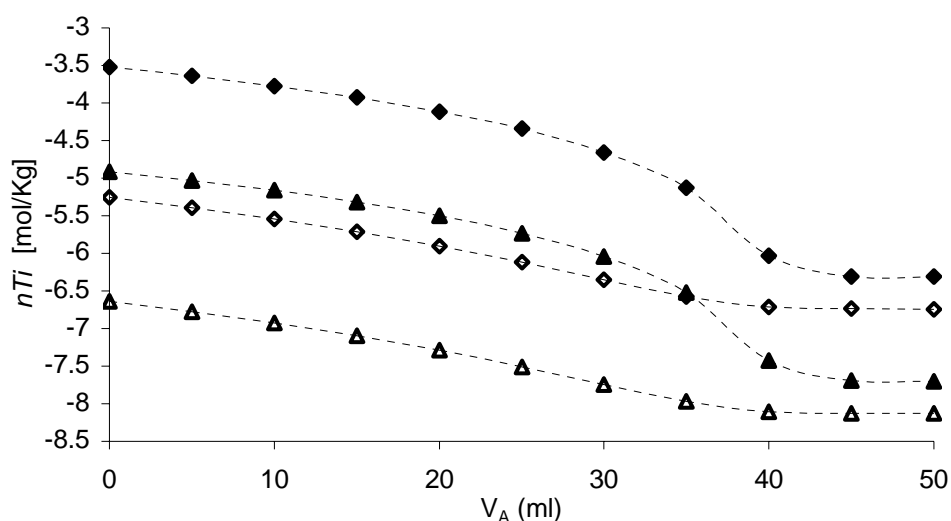


Figure S3. Solubility of TiO_2 as a function of the volume of ammonia solution under hydrothermal conditions calculated for an overall Ti concentration of 0.45 mol/kg (\triangle : macroscopic crystal, $T=220^\circ\text{C}$; \blacktriangle : macroscopic crystal, $T=160^\circ\text{C}$; \diamond : particle diameter 12 nm, $T=220^\circ\text{C}$; \blacklozenge : particle diameter 12 nm, $T=160^\circ\text{C}$). The quantity n_{Ti} plotted on the y-axis represents the overall amount (mol/Kg) of titanium in solution and takes into account all the aqueous species.

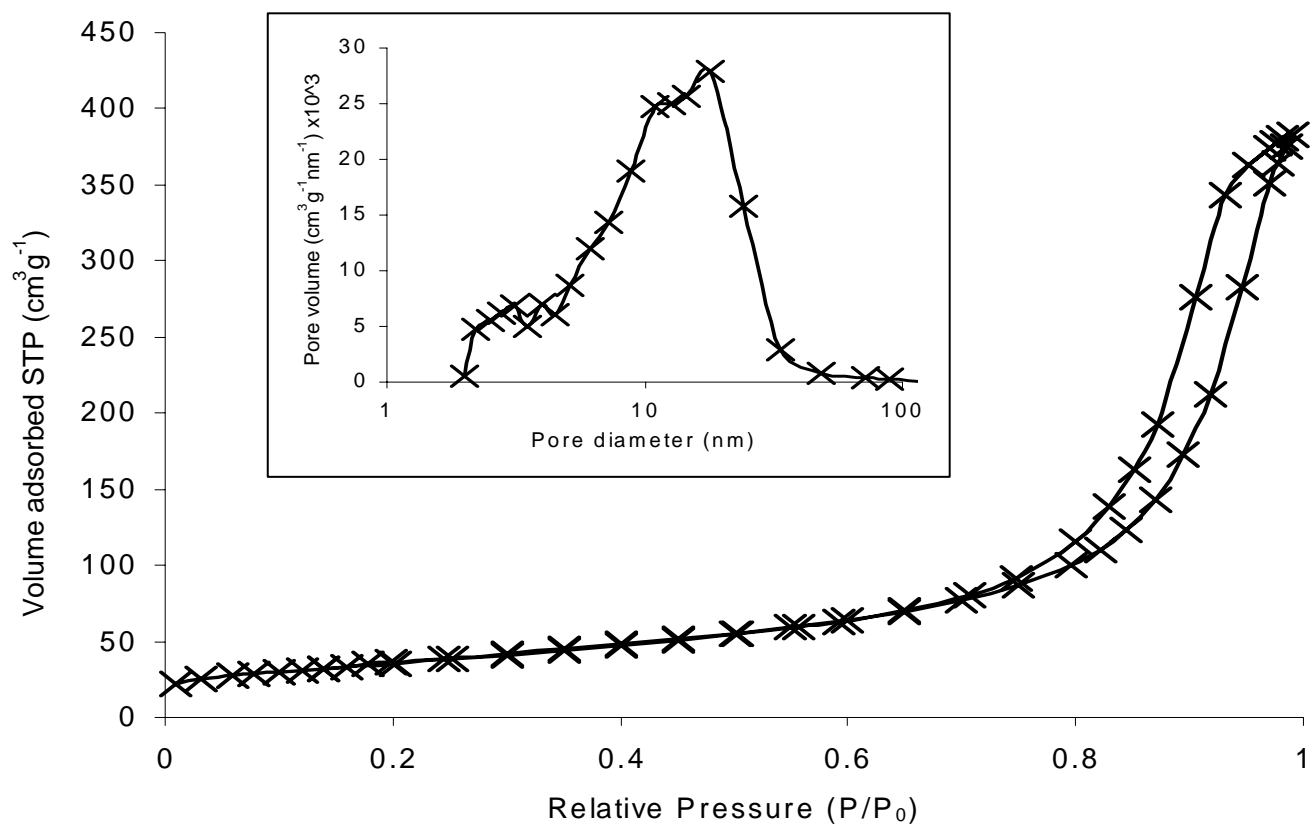


Figure S4. Adsorption/desorption isotherm at liquid nitrogen for sample S12T. The curves correspond to a type IV isotherm with capillary condensation in the mesopores. Inset: pore size distribution.

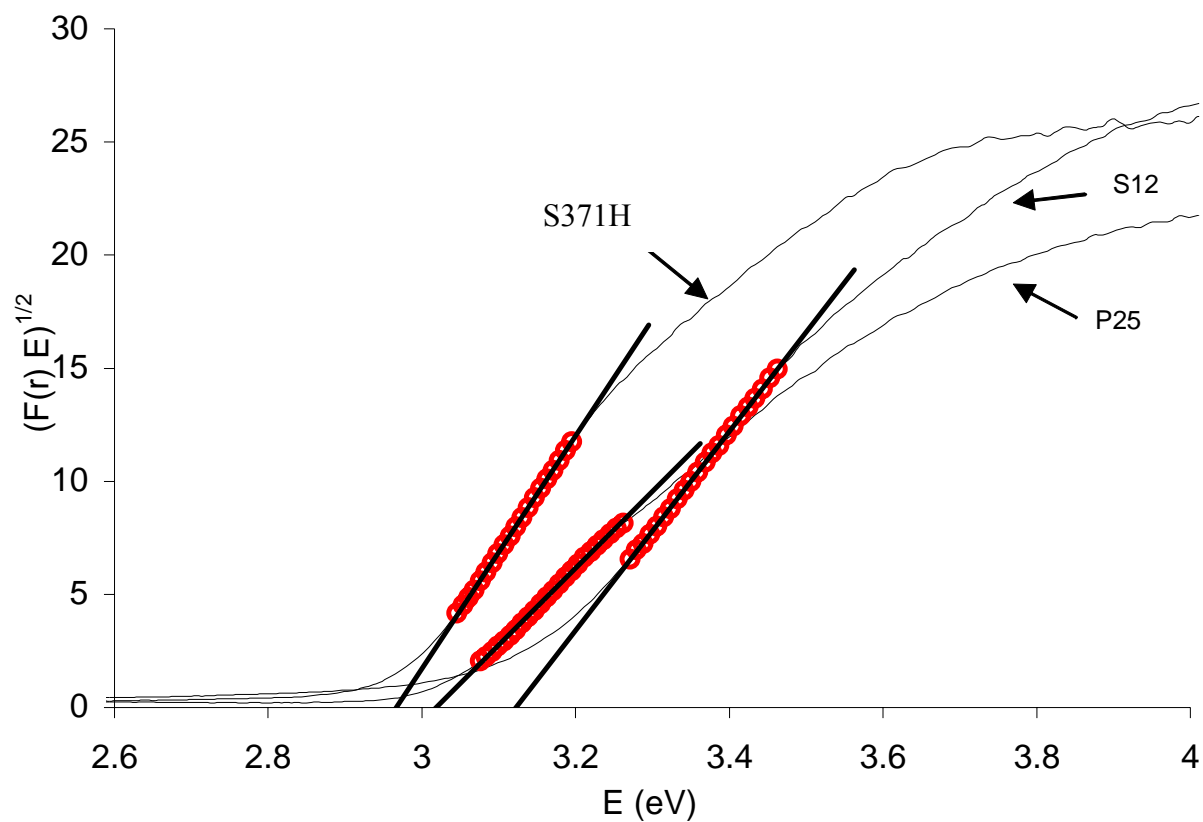


Figure S5. Tauc plot for samples S12 (100% A), S371H (100% R) and Degussa P25. The band gap is evaluated from the intercept with the energy axis of the straight line fitted to the linear portion of the curve.